International Journal of Biological Macromolecules 319 (2025) 145453

Contents lists available at ScienceDirect

International Journal of Biological Macromolecules

journal homepage: www.elsevier.com/locate/ijbiomac

FL30: an epidermal growth factor kinase inhibitor overcoming T790M and C797S mutations through unique conformational modulation mechanism

Elena Romagnoli [a,1], Emiliano Laudadio [b,1], Giovanna Mobbili [a,1], Leonardo Sorci [b], Giovanni Birarda [c], Federica Piccirilli [c,d], Lisa Vaccari [c], Hendrik Vondracek [c,e], Brenda Romaldi [f], Massimo Marcaccio [g], Paola Storici [c], Marta Semrau [c,d], Roberta Galeazzi [a], Andrea Toma [h], Vincenzo Aglieri [h], Pierluigi Stipa [b], Tatiana Armeni [f], Cristina Minnelli [a,*]

[a] Department of Life and Environmental Sciences, Marche Polytechnic University, 60131 Ancona, Italy
[b] Department of Science and Engineering of Matter, Environment and Urban Planning Marche Polytechnic University, 60131 Ancona, Italy
[c] Elettra Sincrotrone Trieste S.C.p.A., 34149 Basovizza, Trieste, Italy
[d] Area Science Park, Padriciano 99, 34149 Trieste, Italy
[e] Diamond Light Source, Harwell Science and Innovation Campus, Didcot, Oxfordshire OX11 0DE, UK
[f] Department of Specialist Clinical Sciences, School of Medicine, Marche Polytechnic University, 60131 Ancona, Italy
[g] Department of Chemistry G. Ciamician, University of Bologna Via Selmi 2, 40126 Bologna, Italy
[h] Istituto Italiano di Tecnologia, Via Morego 30, 16163 Genova, Italy

ARTICLE INFO

Keywords:
Cancer
Epidermal Growth Factor Receptor (EGFR)
Flavone
Inhibitors
Tyrosine kinase inhibitors (TKIs)
SEIRA spectroscopy

ABSTRACT

Tyrosine kinase inhibitors (TKIs) targeting the oncogene Epidermal Growth Factor Receptor (EGFR) are widely used in the treatment of non-small cell lung cancer (NSCLC). In this context, the introduction of fourth-generation TKIs has significantly advanced targeted therapy for T790M and C797S EGFR mutations. Current therapeutic strategies are increasingly focusing on the design of orthoallosteric TKIs, which have shown promise in stabilizing the inactive conformation of mutated EGFR. In this context, we report the discovery of FL30, a small molecule with a flavone core that exhibits nanomolar potency against the EGFR-L858R/T790M mutation, even in the presence of the C797S mutation. The IC_{50} comparable to the Osimertinib - one of the most renowned EGFR-TKIs - emphasizes the remarkable success of the design approach. In NSCLC models, FL30 effectively inhibits cancer growth and EGFR phosphorylation selectively in cells with the EGFR mutations. Kinetic studies, molecular modeling, and Plasmon Internal Reflection Surface-Enhanced Infrared Absorption (PIR-SEIRA) microscopy suggests that FL30 binds to the orthosteric site while inducing the transition of the mutant EGFR toward an inactive-like state. These findings highlight FL30's potential for further optimization and propose a novel approach for developing targeted therapies that combine orthosteric binding with allosteric modulation.

1. Introduction

Tyrosine kinase inhibitors (TKIs) have revolutionized the treatment of non-small cell lung cancer (NSCLC) driven by Epidermal Growth Factor Receptor (EGFR) mutations. Nonetheless, like other targeted therapies, TKI treatment often leads to the emergence of on-target drug resistance mechanisms. Consequently, there is an urgent and compelling need to develop novel therapeutic agents that can overcome these challenges. This has driven researchers and pharmaceutical companies to develop new chemical compounds capable of targeting the mutated forms of EGFR [1].

In this context, the mutant-specific changes in the EGFR structure represent the key for designing mutant-selective TKIs [1–4]. Until now, the most studied EGFR mutated forms include the L858R/T790M double mutant (EGFR-LT); the development of reversible inhibitors (1st and 2nd TKIs generation) effective against EGFR-LT is often hampered by poor selectivity against wild-type (Wt) EGFR, resulting in potentially dose-limiting toxicities and a sub-optimal profile for use in combinations [1]. This led to the development of the 3rd-generation irreversible TKIs, like Osimertinib (OS) or Lazertinib, which covalently bind and alkylate

* Corresponding author.
E-mail address: c.minnelli@staff.univpm.it (C. Minnelli).
[1] Contributed equally.

https://doi.org/10.1016/j.ijbiomac.2025.145453
Received 26 March 2025; Received in revised form 5 June 2025; Accepted 20 June 2025
Available online 21 June 2025

the Cysteine 797 (C797) at the lip of the ATP-binding pocket (Fig. 1A). These TKIs are effective against most clinically relevant EGFR mutants; however, the treatment frequently induces the acquisition of the C797S mutation (20–30 % of cases) leading to tumour relapse in initially responding patients [1,5]. The final challenge in designing TKIs is to avoid cysteine mutations, leading to the development of the 4th-generation of reversible EGFR inhibitors, specifically targeting EGFR L858R/T790M and/or L858R/T790M/C797S mutations, some of which are now entering clinical trials [1]. Overall, this next generation of TKIs differs between them for the recognition site (Fig. 1A-B) and for targeting the active or inactive EGFR conformation, as each conformer possesses distinct characteristics (Fig. 1C) [7–10]. The key differences between the active and inactive EGFR states are the position of the αC-helix and of the DFG motif (D855, F856, G857), the formation or disruption of the salt bridge between the residues Glu (E762) and Lys (K745) (often referred to as the KE salt bridge) and the conformation of the activation loop (A-loop) (Fig. 1C). The active EGFR conformation features an extended activation loop, allowing for substrate binding, while the inactive form has a compact activation loop. In the active state, the αC-helix is oriented toward the active site (αC-helix "in"), which stabilizes the structure and promotes the formation of the KE salt bridge; in the inactive state, it is shifted away (αC-helix "out") resulting

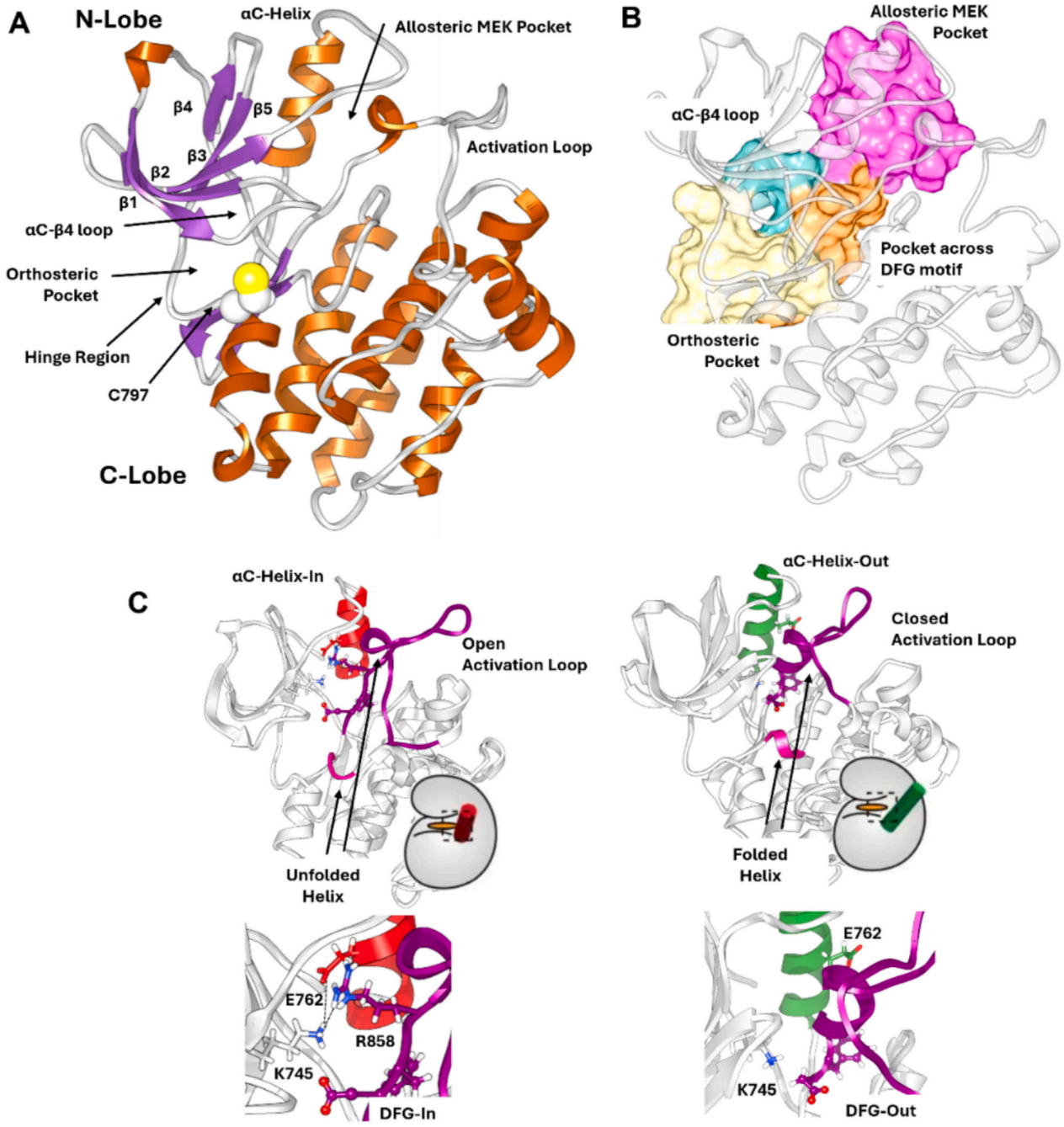

Fig. 1. **(A)** Tyrosine kinase domain of the EGFR in which loops, αC-helix and b-sheets are colored in grey, orange and purple, respectively. **(B)** Type I TKIs bind to the ATP binding pocket (orthosteric site, yellow colour) while type II inhibitors bind mainly the back pocket across the DFG motif (orange colour) in the DFG-out conformation. In contrast, allosteric inhibitors target distinct allosteric pockets. Type III binds to the allosteric site next to the ATP-binding pocket (MEK pocket, magenta colour). MEK pocket is located between the αC-helix and activation loop, and it is accessible mainly in the active EGFR form. The αC-β4-loop represents the interface between orthosteric and allosteric MEK pocket. **(C)** Conformation of Wt and EGFR-LT obtained after molecular dynamics simulations [11].

in the disruption of the KE salt bridge. Additionally, the DFG motif in the active form is in an "in" position, promoting active site accessibility, whereas in the inactive state, it adopts an "out" position, hindering substrate access.

The 4th generation TKIs can be classified into two primary types based on their binding sites: orthosteric and allosteric inhibitors which bind competitively to the ATP binding site, or to other pockets, respectively [1].

In the landscape of allosteric mutant-selective TKIs for the EGFR, the most interesting is the Type III TKIs which occupies the allosteric MEK pocket, located between the αC-helix and the A-loop mainly accessible in the presence of activating mutations such as LT (Fig. 1A-B). In fact, many studies, including ours, demonstrated that these mutations can destabilize the inactive conformation of EGFR, promoting its active state and exposing the allosteric pocket [11,12]. The consequent binding of these allosteric inhibitors induced the transition of the αC-helix from αC-in to the αC-out conformation, preventing kinase activation [13]. However, in the cellular context, allosteric compounds are ineffective as single agents due to the asymmetric ligand-induced dimerization of EGFR [14]. In the past, researchers explored the use of allosteric inhibitors alongside antibodies like cetuximab, which interferes with dimer formation. However, cetuximab is not specific for EGFR-mutants, thereby resulting in on-target wild-type EGFR-mediated toxicities [15]. Current research is now focusing on dual targeting approach to both the orthosteric and allosteric binding sites of EGFR. This approach includes the coadministration of ATP-competitive and allosteric inhibitors, such as Osimertinib with JBJ-04-125 [16], JBJ-09-063 [17] or EAI-432 [18]. The combination of these two drugs increased potency compared to monotherapy and to a delay in orthosteric drug-resistance. Recently, the structural proximity of the MEK allosteric and orthosteric binding sites has led to the development of ATP-allosteric bivalent TKIs [19–22]. They are designed with a specific linker connecting the known TKIs, orthosteric and allosteric. As proof of concept, these bivalent inhibitors can function as ATP-competitive inhibitors while also stabilizing the αC-helix of the kinase in the inactive conformation (αC-out). Current synthetic strategies are focused on optimizing the design of these linkers, as their length, structure, and flexibility are crucial for achieving a super-additive effect that enhances binding to both sites. Despite the promising potential of this approach, a significant challenge remains: the high molecular weight of these compounds can hinders their bioavailability.

Therefore, there is significant interest in finding small compounds (molecular weight of 500 g/mol or less) that can reversibly bind to the orthosteric site of constitutively active mutants EGFR while inducing the transition of the protein into an inactive state. CHMFL-EGFR-202 is a TKI that favors the adoption of an αC-helix-out conformation associated with inactive EGFR; however, it is an irreversible orthosteric inhibitor that forms a covalent bond with the C797 residue (**Fig. S1A—B**) [23,24]. Conversely, the Osimertinib binding to EGFR L858R, T790M, and L858R/T790M stabilized an intermediate active state characterized by a αC-helix-in conformation [25]. There are instances of TKIs that allosterically promote the transition of the A-loop from an open to a closed state, such as in the Src-family kinase Fgr (TL02–59) [26], while other TKIs can induce a distinct DFG-out inactive conformation, as observed in the ALK kinase (001–017) [27]. Currently, there no evidence supporting the existence of reversible orthosteric EGFR-TKIs that operate through similar mechanisms. This gap highlights a significant opportunity for further investigation and innovation in the development of targeted therapies for EGFR mutations.

In this study, we introduce **FL30**, a novel small molecule featuring a distinct chemical scaffold and mechanism of action that set it apart from existing EGFR-TKIs. Traditional EGFR inhibitors primarily rely on flat heteroaromatic cores—such as the anilinopyrimidine scaffold found in third-generation compounds like Osimertinib (which contains a 2-anilinopyrimidine core) and fourth-generation reversible inhibitors like Brigatinib and TQB3804 (characterized by a 2,4-bis-anilinopyrimidine core). In contrast, allosteric fourth-generation TKIs, such as EAI045 and JBJ-04-125-02, are mainly built around an oxoisoindoline phenylacetamide core, which enables them to bind to allosteric MEK sites on the kinase (Fig. 1). These scaffolds are well-known and widely used to optimize existing inhibitors [1]. Compared to currently clinically trialed EGFR-TKIs, **FL30** features a flavone-based core—a flat heteroaromatic system that can be easily functionalized, allowing fine-tuning of its binding properties. Mechanistically, **FL30** showed a unique mechanism of action. Unlike allosteric inhibitors that target non-ATP sites to inactivate EGFR, or covalent inhibitors such as CHMFL-EGFR-202 that stabilize the inactive conformation through covalent binding, **FL30**'s mechanism involves reversible, ATP-site binding that promotes the change in receptor conformation favoring its inactivation. Overall, **FL30** uniquely combines the conformational modulation characteristic of allosteric agents with the reversible binding of orthosteric inhibitors. This dual feature broadens its activity spectrum and enables effective receptor inactivation while potentially reducing resistance development. In terms of selectivity, **FL30** demonstrates a strong preference for mutant EGFR variants over the wild-type receptor, outperforming third-generation agents like Osimertinib and fourth-generation TKIs such as Brigatinib and TQB3804. Due to its unique chemical structure, mode of action, and enhanced selectivity for mutant EGFR variants, **FL30** emerges as a promising candidate for further in vivo investigation and optimization. This potential may expand the landscape of EGFR-TKIs available for the treatment of NSCLC patients.

2. Results and discussion

2.1. Rational identification of lead compounds and synthesis of amide-containing flavone derivatives

Recent structural studies, including ours, highlight the importance of reversible orthosteric EGFR drugs to form stronger reversible interactions within ATP-binding pocket of the kinase domain in mutant EGFR. This enhancement is essential for improving their potency and selectivity [12,28–32]. Key regions of focus can include: (i) hinge region, as it is where many ATP-competitive agents anchor themselves; (ii) K745, the conserved catalytic residue involved in the formation of salt bridge and essential for maintaining EGFR in its active conformation; (iii) T854, which interaction appears to be a structural feature of the most potent 4th-generation orthosteric TKIs and (iv) T790M, the mutated gatekeeper residue known for enhancing ATP affinity and blocking the binding of reversible ATP-competitive TKIs through a steric effect. In addition to these considerations, we want eventually to explore additional interactions with residues localized in the αC-β4 loop (V774, C775, R776). Considering that the irreversible TKI CHMFL-EGFR-202 interacts with this poorly explored region stabilizing an inactive EGFR conformation (**Fig. S1B**), we hypothesized that targeting this site can potentially destabilize the near αC-helix conformation.

For the design of new inhibitors, flavone was used as a scaffold (Fig. 2A). Previously, starting from this structure, we successfully developed a selective TKI inhibitor for the mutated forms of the receptor (Fig. 2B), but its efficacy was in the low micromolar range. The goal is to achieve a TKI that is effective in the nanomolar range and has improved selectivity for the mutated forms compared to the wild type. In this context, various groups have been added to promote interactions with the previously described regions, while also trying to maintain the interaction of the flavone with C775 in the αC-β4 loop (Fig. 2C).

Each newly designed compound underwent a dual-track focused docking analysis to identify those with a higher affinity toward the active EGFR-LT mutated form (checked for DFG-in, αC-helix-in, extended A-loop), targeting nanomolar activity ($E_{binding} < -10$ kcal/mol), while ensuring that the Wt form was less favorable ($E_{binding} > -7$ kcal/mol) (**Fig. S2**). Compounds that showed interactions with the selected regions were thoroughly examined. This is a common strategy applied to avoid loss of information after virtual screening [31,33]. Among the most promising candidates, we identified a series of

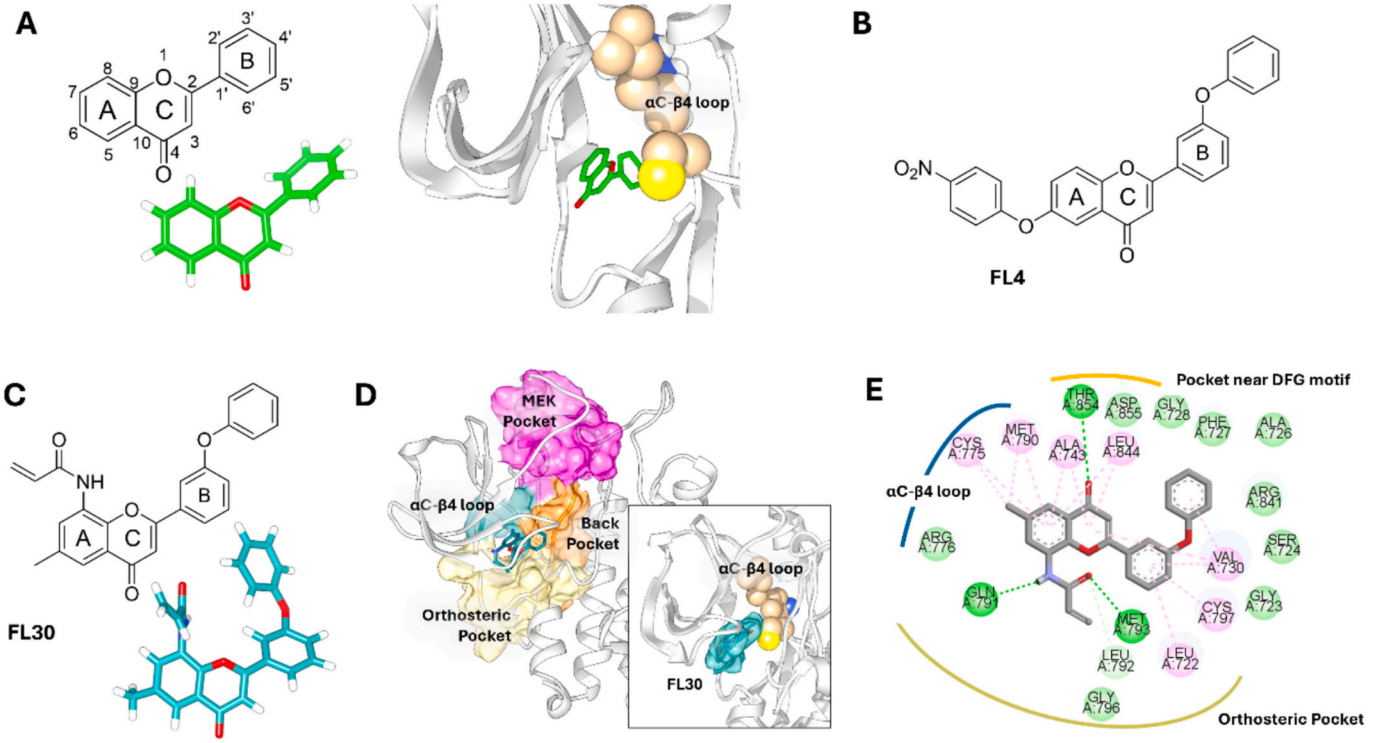

Fig. 2. **(A)** Left: 2D and 3D Chemical structure of flavone scaffold. Right: Binding pose of flavone inside the EGFR-LT. The residues in the αC-β4 loop region (V774, C775, R776) are shown as spheres colored in tan. **(B)** 2D Chemical structure of FL4, a flavone-based EGFR-TKI previously identified [31]. **(C)** 2D and 3D Chemical structure of **FL30**. **(D)** Tyrosine kinase domain of the active EGFR-LT (checked for open A-loop, DFG-in, αC-helix-in and unfolded helices in the A-loop) [11] docked to **FL30**: surface representation illustrating the position of **FL30** in relation to various binding pockets. Inset: interaction of **FL30** with the αC-β4 loop. **(E)** Detailed depiction of the binding mode of **FL30** in complex with EGFR-LT, drawn by Discovery Studio 4.5. The hydrogen bond, CH-hydrogen bond, and π-alkyl and VdW interactions are highlighted in green, light-green and pink, respectively.

compounds exhibiting strong binding affinity toward EGFR-LT ($E_{binding} \leq -11$ kcal/mol). They feature an amide moiety attached to the C8 position of the A ring and a phenoxy group linked to the C3' position of the B ring.

To validate the in silico design and screening, selected amide-containing flavones were synthetized: **FL30**, **FL31**, **FL32**, **FL33** and **FL34**. The structures are shown in Scheme 1. Initially, we obtained **3a** and **3b** intermediates from the reaction between 1-(2-hydroxy-5-methyl-3-nitrophenyl)ethanone (**1a**) or 1-(2-hydroxy-5-methoxy-3-nitrophenyl) ethanone (**1b**) and 3-phenoxybenzaldehyde (**2**) under basic conditions.

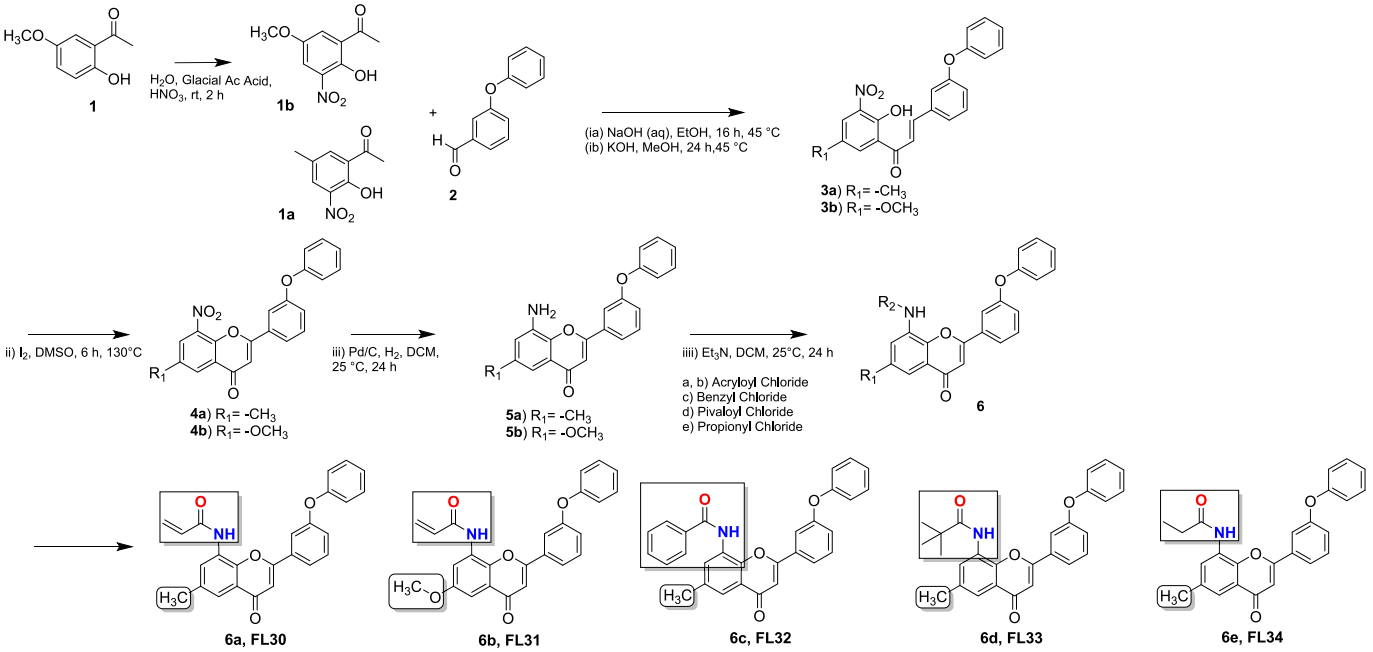

Scheme 1. Chemical steps in the synthesis of FL-derivatives.

Then, the ring C closure mediated by iodine led to the nitroflavone intermediates (**4**), which were then selectively reduced to their corresponding amine flavone derivatives using H_2 and palladium on carbon (Pd/C). Subsequently, the -NH_2 group of the amine derivatives was acylated with the appropriate acyl chloride to yield the final amide flavone derivatives.

2.2. Reversible and selective inhibition of EGFR mutants by FL30

Flavone analogues were first screened in a biochemical assay at a single concentration of 1 μM against EGFR-LT. Although **FL31**, **FL32,** and **FL33** showed the ability to inhibit EGFR activity (20–30 % of inhibition), the higher potency was obtained with **FL30** which showed almost complete inhibition at the concentration tested (92 % of inhibition) (**Fig. S3**). Analyzing the binding mode of the **FL30**, we can observe that **FL30** binds to the orthosteric site, extending toward both the αC-β4 loop and to the back pocket near the DFG motif (Fig. 2C-E). More in detail, the acrylamide moiety of **FL30** plays a pivotal role by anchoring the compound to the hinge region of the protein. This anchoring is facilitated through a bidentate hydrogen bonding with the backbone amide of M793 and Q791 in addition to a carbon-hydrogen bond with the side chain of L792. A network of hydrophobic interactions, primarily involving π-CH interactions, significantly enhances the overall stability of **FL30**'s binding. In this context, interactions with catalytic spine residues were observed, including L844, A743, and A726, along with additional support from L722, V730, and C797. These interactions stabilize **FL30**, creating a hydrophobic pocket and increasing the binding affinity. The phenyl ring A and the methyl group at C6 make further hydrophobic π-CH interactions with C775 and form van der Waals interactions with R776, which is located within the αC-β4 loop. Notably, the mutated gatekeeper residue, M790, also participates in the stabilization of ring A (Fig. 2D**).** The flat heteroaromatic system (ring C) is stabilized through a hydrogen bond with T854, which is located before the activation loop. This interaction contributes to the binding stability of **FL30,** suggesting potential implications for the dynamics of the activation loop, which may be influenced by the **FL30** presence. Finally, several van der Waals interactions with the residues belonging to the glycine-rich P-loop were observed (G723, G726, G728, F727). Interestingly, when the acrylamide group was replaced with either a benzyl group (**FL32**) or a pivaloyl group (**FL33**), the resulting derivatives predominantly extended their binding within the pocket near the DFG motif, thus losing the interaction with the αC-β4 loop region (**Figure S1C**). Furthermore, replacing the methyl group at C6 of ring A, which participates in hydrophobic π-interactions with C775, with a larger and more polar methoxy group allowed the flavone to adopt a binding mode similar to that observed for **FL32** and **FL33**. The complete inability of **FL34** to inhibit EGFR-LT kinase activity (**Fig. S3A**) further emphasizes the essential role of the acrylamide group in **FL30**'s activity. As shown in **Fig. S1D**, hydrogenation of the double bond between Cα and Cβ of the amide (**FL34**) causes the compound to shift out of the ATP-binding pocket, leading to a loss of hinge interactions. The saturation of the Cα–Cβ double bond alters the conformation of the amide group, increasing the flexibility of the entire moiety, which consequently impacts its binding affinity. Overall, our findings showed that both the flexibility and conformation of amide derivatives are pivotal in dictating the spatial orientation and interactions of the compounds within these key protein regions.

Considering the obtained results, a dose-dependent assay of **FL30** was performed and compared with Lapatinib and Osimertinib as standard TKIs references for Wt and EGFR-LT, respectively (Table 1). Interestingly, **FL30** exhibited an IC_{50} of 95 nM for EGFR-LT, only marginally higher than the IC_{50} of 87 nM for Osimertinib. Notably, it showed poor efficacy in inhibiting Wt EGFR, with an IC_{50} of 25,000 nM, highlighting its exceptional selectivity for the mutant EGFR. The selectivity index (SI) for Osimertinib relative to Wt EGFR was approximately 58, consistent with findings from other studies aligning with reported ranges of 40 to 100 in other studies [21,30,34]. In contrast, **FL30** boasted a selectivity index of 257, which is four times greater than that of osimertinib. Furthermore, comparisons with the previously identified flavone-based EGFR-TKI (**FL4,** Fig. 2B) [31], showed that the design approach led to a more potent and selective compound.

Table 1
IC_{50} values for the EGFR Wild type (Wt), L858R/T790M (LT) and L858R/T790M/C797S (LTC) in an enzyme-based assay.

Compd	Kinase activity (IC_{50}, nM)				
	Wt	LT	LTC	SI[a]	SI[b]
FL4	>150,000	12,000 ± 1259	16,000 ± 2324	>13	>9
FL30	25,000	95 ± 11	320 ± 37	257	78
Lapatinib	5 ± 0,9	12,000 ± 604	20,000	–	–
Osimertinib	5000 ± 1324	87 ± 7	>10,000[c]	58	0.5
Erlotinib	n.d.	2711 ± 530	n.d.	–	–

[a] Selective Index (SI), determined as the ratio between IC_{50} values measured in Wt and IC_{50} calculated in LT.
[b] Selective Index (SI), determined as the ratio between IC_{50} values measured in Wt and IC_{50} calculated in LTC.
[c] Inhibition was <50 % at the highest used concentration (i.e., 10 μM).

Although the design was performed on the EGFR-LT, we sought to determine **FL30**'s effectiveness in inhibiting the EGFR L858R/T790M even in the presence of C797S mutation, which arises from treatment with irreversible inhibitors. As outlined in the Table 1, **FL30** exhibited potent binding and inhibition of the EGFR L858R/T790M/C797S (LTC) variant in the nanomolar range (IC_{50}, 320 nM). In this case, the potency of **FL30** was found to be significantly higher than that of Osimertinib, which has an IC_{50} higher than to Wt (>10,000 nM). These findings align with existing literature [34–36] and confirms that the Cys797 mutation renders this drug largely ineffective. Additionally, **FL30** demonstrated a commendable selectivity index of 78 (Table 1), supporting its potential as a promising new chemical entity capable of overcoming both the T790M and C797S resistance mutations. Compared to several fourth-generation TKIs currently under development, **FL30** exhibited greater selectivity for mutants EGFR than to wild-type EGFR. For example, orthosteric EGFR-TKIs TQB3804 targeting LT had an SI of approximately 6, while Brigatinib demonstrated an SI of about 10 for LTS [1]. Similarly, the allosteric EGFR-TKI JBJ-04-125-02 showed SI values of 8 and 9 for LT and LTS, respectively [30]. This discovery opens avenues for further investigation into **FL30**'s therapeutic potential in treating resistant EGFR mutant cancers.

The inhibition of the mutant form containing the C797S mutation also suggests that **FL30** is not an irreversible TKI; to explore this aspect, we conducted experiments to evaluate the reversible nature of **FL30**. One of the hallmark characteristics of covalent inhibitors is their time-dependent inhibition of the target protein [37]. Our kinetic analysis revealed no significant change in the IC_{50} value for EGFR-LT after 45 min of preincubation with **FL30** (**Fig. S3**). This stability in the IC_{50} value indicates that **FL30** likely operates through a reversible mechanism involving noncovalent interactions.

To evaluate potential off-target effects, we tested **FL30** at a concentration of 1 μM against a panel of nine representative kinases. This included kinases with accessible and reactive cysteine residues within or near their ATP-binding sites, such as JNK2 (C116), BTK (C481), ERK2 (C164), FGFR4 (C552), and AKT1 (C310), for which irreversible inhibitors containing an acrylamide group have been previously developed [38–42]. In addition to these cysteine-rich kinases, we included three other kinases—ALK, CDK2, and MET—in our profiling to gain a broader understanding of potential off-target interactions. As shown in Table 2, the results demonstrated that FL30 exhibited minimal off-target activity; specifically, it did not significantly inhibit JNK1, ERK2, or AKT1. For kinases like BTK and FGFR4, only about 10 % inhibition was observed at the tested concentration, indicating high selectivity. Similarly, no substantial inhibition was detected for ALK, CDK2, or MET. Overall, this targeted kinase provides an initial assessment of **FL30**'s

Table 2
Residual activity values for **FL30** at 1000 nM in singlicate in 10 kinase assays. All values are calculated as % of control.

Compound ID	Targetable cysteine	FL30 (1000 nM)	Staurosporine (1000 nM)
JNK1	C116	102	36
BTK	C481	89	5
ERK2	C164	108	57
FGFR4	C552	89	12
AKT1	C310	107	9
ALK	–	99	1
ALK C1156Y	–	101	1
CDK2/CycA1	–	100	0
MET	–	100	23

selectivity and off-target activity, supporting its potential safety profile.

2.3. FL30 Inhibits the activation of EGFR L858R/T790M in NSCLC models

The antiproliferative activity of **FL30** was assessed against a panel of cell lines with different EGFR status: NSCLC H1975 (EGFR-L858R/T790M), NSCLC A549 (showing high expression level of Wt EGFR), MCF7 (showing low expression level of Wt EGFR) and human fibroblast cells (HDF) as a model of non-cancer cells (**Table S1** and Fig. 3A). The **FL30** displayed a high antiproliferative effect on H1975 cells (IC_{50} values of 1.7 μM) while showing low cytotoxicity on Wt EGFR cells (A549; 31-times lower than to H1975), which is consistent with the mutant selectivity observed in the enzyme-based assay described below. Additionally, a cell-based target validation performed on the MCF7 further supports the conclusion that the **FL30** is not effective against Wt EGFR (**Table S1** and Fig. 3A). Interestingly, the IC_{50} observed in H1975 cells is lower than that of a recently published bivalent TKI, which reported an IC_{50} of 3 μM [43]. Flow cytometry results corroborated the ability of **FL30** to function as a mutant-selective TKI (Fig. 3). In the H1975 cells, after 4 h of treatment with 1 μM and 5 μM concentration of **FL30**, there was a notable 60 % and 80 % reduction in EGFR phosphorylation level compared to untreated cells, respectively (Fig. 3B, D). No effects were observed in cells expressing Wt EGFR (Fig. 3C, D). Therefore, these data underlined the potential of **FL30** as novel reversible and mutant-selective TKIs.

2.4. FL30 induces the transition of the mutated EGFR from active to an inactive-like state

2.4.1. SEIRA reveals conformational changes induced by FL30

Surface enhanced infrared absorption (SEIRA) spectroscopy was used to study the EGFR secondary structures combining infrared microscopy with advanced plasmonic devices, which are engineered to resonate at specific frequencies corresponding to the vibrational modes of protein's peptide backbone. This resonance amplifies the infrared signal with respect to traditional infrared spectroscopy, allowing subtle structural changes in proteins to be discerned while interacting with other biomolecules [44–46]. One of the main advantages of SEIRA spectroscopy is its capacity to study enzyme-inhibitor interactions in conditions that closely resemble the natural environments of biological systems and in a dynamic way. In our recent studies, we showcased the effectiveness of SEIRA microscopy in detecting structural differences in the secondary structure of the inactive (Wt EGFR) and the active (EGFR-

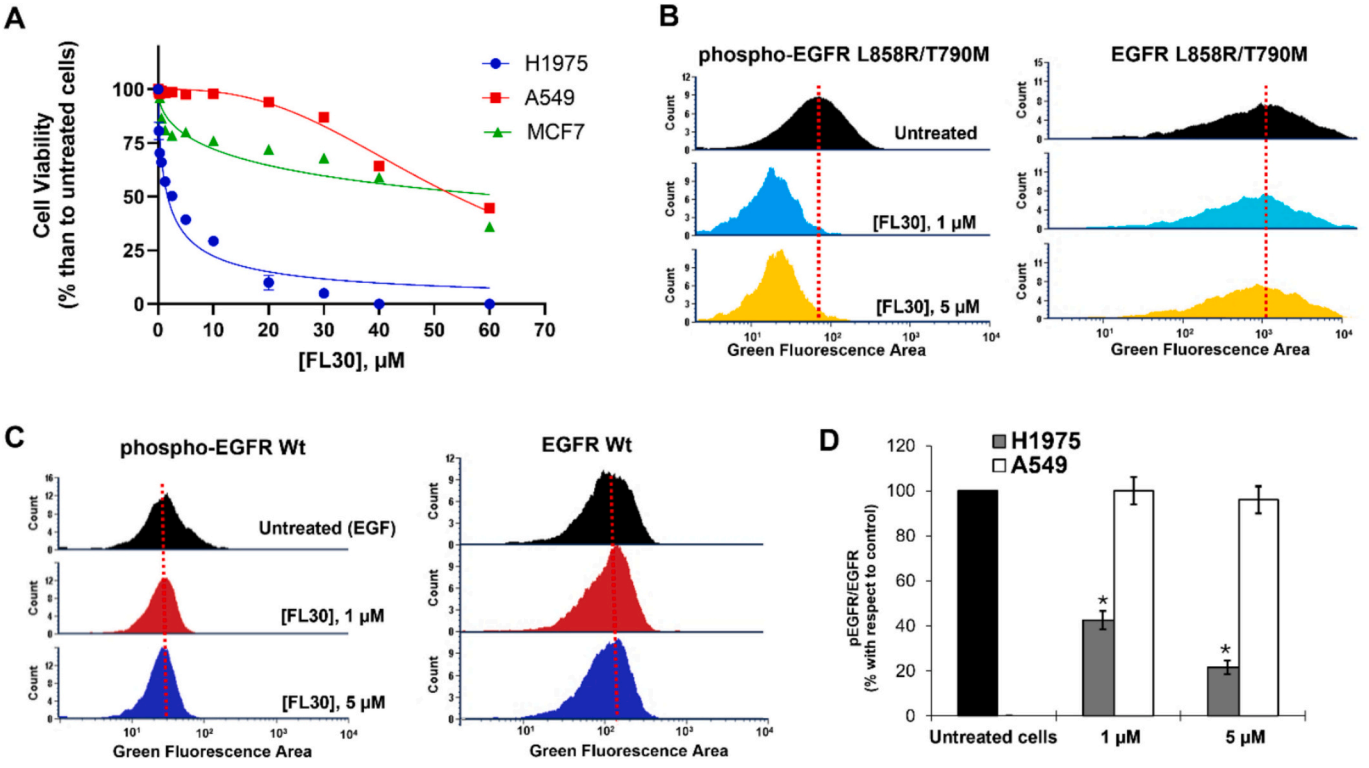

Fig. 3. (A) Antiproliferative activity of **FL30** on a panel of cells with different EGFR status. Cells were treated with increasing **FL30** concentrations, and the cell viability was assessed by using XTT assay. Relative IC_{50} values were determined by non-linear regression analyses using GraphPad Prism 10.4.1(627), employing [Inhibitor] vs normalized response model. **(B—C)** The effect of **FL30** on the EGFR phosphorylation by Flow cytometry. Data are analyzed with FCS 7 Express: **(B—C)** Representative FACS showing phospho-EGFR and total EGFR levels with and without compounds in H1975 (EGFR L858R/T790M) and A549 (EGFR Wild type) NSCLC cells; **(D)** Histogram representing the percentage of phospho-EGFR normalized to total EGFR levels in H1975 and A549 NSCLC cells after **FL30** treatments for 4 h and analyzed by flow cytometry by using antibody against phospho-EGFR (Tyr1068). The percentage values derived from the ratio between the geometric mean fluorescence intensity of the phospho-EGFR to the total EGFR. Representative FACS showing total EGFR levels after compounds treatment and data derived from flow cytometry analyses are shown in SI (Table S2). *$P < 0.001$ vs. untreated cells.

LT) conformation of EGFR [11]. As previously described, the inactive form of EGFR adopts a closed conformation, while the active form assumes an open conformation. These structural differences are reflected in the SEIRA spectra, particularly in the regions associated with helices and loops [11]. Given SEIRA' ability to differentiate between these two conformations, we conducted kinase binding assays to gain insight into the binding mechanisms and the structural adaptations induced by the **FL30** binding in the absence of ATP.

The target proteins, Wt EGFR and EGFR-LT were immobilized on a plasmonic chip, and SEIRA measurements in the 1490–1710 cm^{-1} range of the Wt and EGFR-LT monolayers were acquired in Plasmonic Internal Reflection (PIR) configuration (Fig. 4**A, D**). Following this, a solution containing **FL30** at a concentration equivalent to its IC_{50} value was injected and flowed over the surface to facilitate the formation of the EGFR-TKI adduct. The IR data were then compared after processing. Overall, the spectral analysis conducted before and after the incubation of **FL30** with both Wt (Fig. 4**B—C**) and EGFR-LT (Fig. 4**E-F**) clearly demonstrated **FL30** ability to induce conformational changes selectively in the mutated EGFR-LT form.

Analyzing the average spectra, the frequency associated with the α-helices shifts from 1660 to 1657 cm^{-1} when LT is treated with **FL30**, approaching the value measured in the Wt EGFR (~1652–1655 cm^{-1}). No appreciable shift is instead observed for Wt + **FL30,** implying that the conformational response to **FL30** is specific to the LT mutant**.** This change is consistent with a transition toward a more hydrated and less compact structure. In Laudadio et al. [11], SEIRA and MD analysis showed that activating mutations like LT shift the Amide *I* band to higher wavenumbers (~1660 cm^{-1}), associated with a hyper compacted, catalytically active α-helix (**Fig. S4**). Interestingly the effect of **FL30** on EGFR-LT appears more pronounced and dynamic, suggesting a structural response to binding that includes α-helix relaxation and increased hydration, hallmarks of a transition toward an inactive, therapeutically relevant conformation. In line with this evidence, in our previous work [44], we observed only minor changes in the Amide *I* region of EGFR-Wt upon Lapatinib treatment (~1654–1656 cm^{-1}), with minor structural changes. This is consistent with the findings of Wood et al. [47], who demonstrated that Lapatinib binds to an inactive-like conformation of wild type EGFR, shifting the α-helix to a more solvent-accessible environment without inducing substantial secondary structure changes.

The differences in structural dynamics were further elucidated through Principal Component Analysis (PCA), whose scores for Wt and LT are reported in the scatterplots in Fig. 4**C**, **F** and the loadings in **Fig. S5** respectively. The interaction with **FL30** produced non-significant effects on Wt structure confirming the mutant-selective interaction of **FL30** to EGFR-LT. Conversely, Fig. 4**F** illustrates a clear separation of data along both Principal Component 2 (PC2) and Principal Component 3 (PC3) for the LT monolayer treated with the inhibitor **FL30**. The box plots presenting paired comparisons utilizing Tukey's test for score values of PC2 and PC3 (**Fig. S5D—F**) corroborate these findings, revealing that, for EGFR-LT in the presence of **FL30**, both PC2 and PC3 distributions significantly differ from those of EGFR-LT alone ($P \leq 0.001$ for PC2 and PC3). The spectral shape of PC2 in the region of Amide *I* band suggests the data separation to be driven by negative peaks at 1646 cm^{-1} and a positive one at 1668 cm^{-1}. While the first contribution may be attributed to loops and short strands, the second one is assigned to 3(10)-helix and β-turns [48–51]. A third peak at 1692 cm^{-1} is also prominent, but it cannot reliably be assigned based on literature data. PC3 instead presents a strong negative peak at 1646 cm^{-1} (associated with loops or strands) and a strong positive peak at 1615 cm^{-1}. This later peak is possibly related to CC stretching and CH bending of tyrosine amino acid side chain, and the correlated PC3 peak at 1506 cm^{-1} supports this attribution [52]. Overall, the analysis underscores significant structural alterations within the loops, helical conformations and β-turns following interaction with **FL30**, predominantly captured by PC2 (Fig. 4**E and Fig. S5D**). In contrast, PC3 accounts for more subtle modifications in the loops and short β-strands possibly adjacent to the ATP-binding pocket confirming that **FL30** binds within the orthosteric site which certainly cause subtle conformational changes around the pocket to accommodate the ligand.

In addition, we also compared SEIRA results with the previously identified flavone-based inhibitor, **FL4**, which selectively inhibits EGFR-LT activation via only an ATP-competitive mechanism with an IC_{50} of 10 μM [31]. Similar to **FL30**, **FL4** did not induce significant conformational changes in Wt EGFR, confirming its mutant-selective nature (**Fig. S6A—D**). For the EGFR-LT + **FL4** complex, we did not observe separation along PC2, indicating no alterations in helical conformations and β-turns. As expected, we noted a partial separation along PC3 ($P \leq$

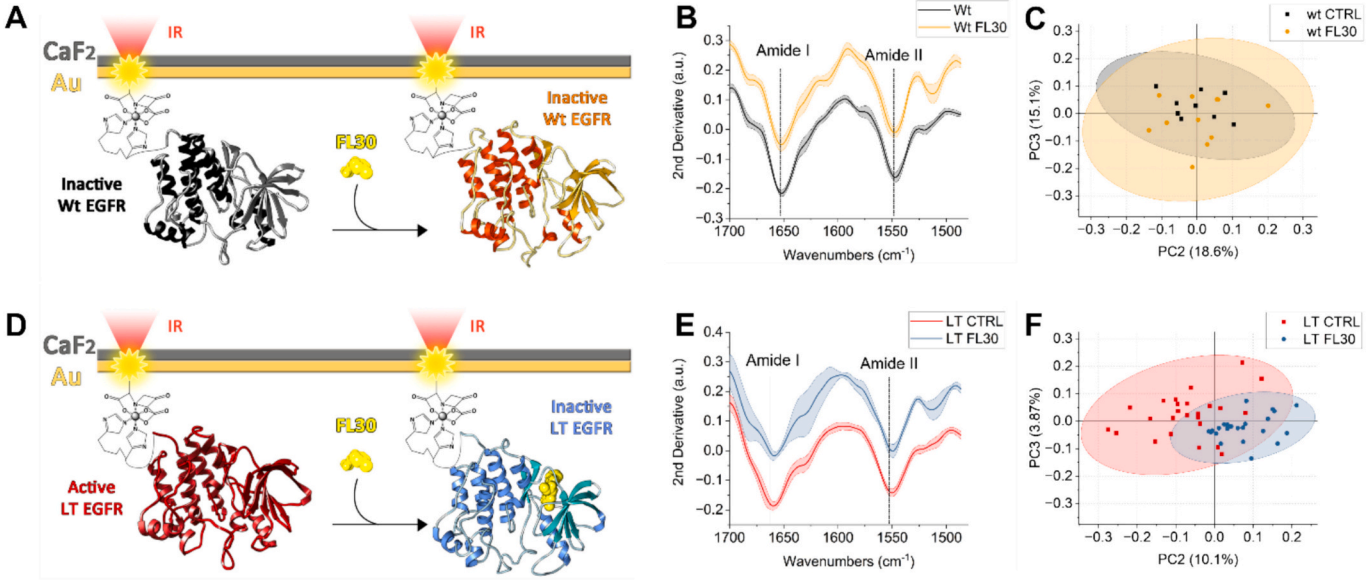

Fig. 4. (A-D) Overview of the experimental conditions and results obtained by SEIRA spectroscopy. **(B)** Average spectra of Wt and Wt + **FL30**, shadowing is the SD of the different measurements. **(E)** Same plots for the EGFR-L858R/T790M (LT) experiments. **(C)** Scatterplot representing the PCA score values of all the experimental points of the Wt + **FL30**, the ellipses represent the C·I of 95 %. **(F)** Scatterplot representing the PCA score values of all the experimental points of the EGFR-LT + **FL30**, the ellipses represent the C·I of 95 %.

0.001), reflecting subtle modifications in loops and short β-strands near the ATP-binding pocket (**Fig. S6E—H**). Collectively, these findings indicate that both **FL30** and **FL4** interact with the ATP-binding pocket of EGFR. However, **FL30** not only binds to this site but also destabilizes the active conformation of the receptor, offering valuable insights into its potential role in modulating EGFR activity.

2.4.2. FL30 induces the EGFR-LT toward an inactive-like conformation: Molecular dynamics simulation

Considering the SEIRA results about the EGFR structural modifications, and to gain insights into the mechanism of action of **FL30**, we conducted extensive molecular dynamics (MD) simulations starting from the active-EGFR-LT model used in the docking studies, which features DFG-in conformation, linear conformation of the regulatory spines (R-spines), αC-helix in inward position with the KE salt bridge, and unfolded helices in the A-loop. We monitored the evolution of the structures in the presence of **FL30** and compared the resulting conformations of EGFR-LT alone with those of EGFR-LT-**FL30** during 1 μs of simulation. Notably, distinct conformational changes were observed in EGFR induced by the presence of **FL30** (Fig. 5).

Specifically, we found that **FL30** disturbs the EGFR structure and induces an allosteric modulation of the EGFR-LT structure which results in a transition from open to closed EGFR conformation (Fig. 5A). During this transition, a functionally important third conformation was observed after about 0.2 μs of MD, in which the kinase complexed with **FL30** exhibits local intrinsic disorder or "cracking" in some areas of the protein. As shown in figure, **FL30** promotes a partially unfolded αC-helix, which disrupts the salt bridge between K745 and E762 (Fig. 5B) and disassembles the regulatory spines (R-spines) which are known to be important for the kinase activity (Fig. 5C). Computational and experimental studies have shown that these local "cracking" could facilitate conformational changes by increasing conformational entropy, thereby lowering the free energy of the transition state [53,54]. This phenomenon has been shown in the transition from the active Wt EGFR which is unstable in the absence of an activator [1,11,28,54]. At the same time, the presence of activating mutations such as L858R, the formation of this third intermediate disordered state is suppressed, thereby stabilizing the active conformation and promoting EGFR dimerization and activation. Based on these observations, it appears that **FL30** destabilizes the active EGFR-LT conformation leading to an intermediate disordered conformation, which then promotes the transition to an inactive-like conformation. Measurement of the conformational fluctuations in our EGFR kinase simulations (residue-specific root-mean-square fluctuation, RMSF) showed that the EGFR-LT-**FL30** conformation is characterized by high RMSF values, particularly in the regions of the αC-helix, activation loop, and near the hinge region. Interestingly, these are the same areas that underwent changes in the SEIRA results (**Fig. 4**). In contrast, smaller fluctuations were observed for the EGFR-LT without the ligand (**Fig. S7A)**.

Finally, to provide further confirmation of the action mechanism of **FL30** at a computational level, we conducted a brief molecular dynamics simulation (200 ns) starting from the inactive conformation of EGFR-LT, which has been used in our previous studies aimed at investigating the constitutive activation induced by the T790M and L858R mutations [11]. As extensively described in the previous sections, EGFR-LT in simulation tends to evolve toward an active conformation with the formation of the KE salt bridge. Therefore, we wanted to test the effect of **FL30** on this transition. As can be seen in **Fig. S7C—D**, in the presence of **FL30**, the E762 is rotated out, preventing the formation of the salt bridge between K745 and E762. The radius of gyration (Rg), a measure of the compactness of the EGFR structure, shows a decrease in EGFR-LT, indicating a transition to a more compact active state. In contrast, the presence of **FL30** results in a slight increase in Rg, suggesting that it maintains a more extended and open conformation (**Fig. S7D**). These observations highlight **FL30** ability to modulate the structure of EGFR-LT by inducing and stabilizing an inactive-like conformation.

To elucidate the unique inhibitory mechanism of **FL30** compared to other EGFR inhibitors, a comprehensive in silico comparative analysis was performed between the EGFR-LT-**FL30** complex and a selection of known inhibitors with available crystallographic data. This comparison primarily focused on the conformational states of the EGFR protein within each complex.

Firstly, when comparing **FL30** to ATP-competitive reversible TKIs such as Brigatinib (PDB: 7ZYM), a distinct binding mode is evident. Brigatinib, initially developed as an ALK inhibitor, inhibits mutant forms of EGFR like L858R/T790M/C797S by binding within the ATP-binding pocket. Structural analysis shows that Brigatinib interacts via hinge region anchoring, characteristic of ATP-competitive inhibitors, maintaining the kinase in an active conformation where the αC-helix remains inward-facing (Fig. 5D), and key residues K745 and E762 form the canonical KE salt bridge. In contrast, the EGFR-T790M/V948R in complex with the allosteric inhibitor JBJ-09-063 (PDB: 7JXQ) displays a similar conformational profile of the EGFR-LT-FL30 complex: the αC-helix adopts an outward conformation, indicative of an inactive, open state (Fig. 5E). However, the allosteric inhibitor JBJ-09-063 occupies the MEK binding pocket, while **FL30** binds within an orthosteric site. Instead, the binding mode of **FL30** shows also some similarities to that of the inhibitor CHMFL-EGFR-202. As illustrated in **Fig. S1A**, CHMFL-EGFR-202, as **FL30**, interacts with the αC-β4 loop residues (V774, C775, R776) and promotes an inactive EGFR conformation in the L858R mutant. However, while CHMFL-EGFR-202 forms an irreversible covalent bond, **FL30** is reversible, indicating that **FL30** exerts its inhibitory effect through a distinct binding modality. Overall, this data underscores a different mechanism of inhibition, primarily via non-covalent interactions within the orthosteric site, leading to conformational stabilization of the inactive kinase state.

3. Conclusion

In this study, we began with a molecular scaffold featuring a flavone core (**FL**), which has demonstrated significant potential as a template for the design of mutant-selective EGFR-TKIs [31]. By employing structure-based drug design, we successfully discovered a small molecule named **FL30**. This flavone, featuring an amide group, exhibits nanomolar potency for the EGFR-L858R/T790M mutation, even in the presence of the C797S mutation, with a greater efficacy compared to the Osimertinib. Our findings, derived from kinetic analyses, PIR-SEIRA microscopy, and extensive molecular modeling, indicate that **FL30** operates through a distinct mechanism of action. **FL30** binds to the orthosteric site of the active EGFR-LT protein anchoring themselves to the hinge region and seems to interact with the αC-β4 loop, near the allosteric pocket. The interaction with these residues probably disturbs the EGFR-LT active conformation, facilitating the transition of EGFR toward an inactive-like state. However, further evaluation needs to be performed in the future to prove the interaction with this specific region. Remarkably, **FL30** inhibition mechanism is characterized by reverse allosteric communication within the protein, highlighting its unique mode of action. While upcoming structural studies may provide additional insight into the **FL30** mechanism, the current findings compellingly demonstrate **FL30** capability to bind at the orthosteric site and induce significant conformational modulation within the EGFR structure. This dual mechanism—binding at the orthosteric site while simultaneously exerting allosteric effects—not only positions **FL30** as a promising candidate for further optimization but also paves the way for the synthesis and development of other reversible orthosteric inhibitors that can leverage a synergistic therapeutic approach. However, given the substantial differences between in vitro and in vivo conditions, it is essential to conduct in vivo evaluations using relevant animal models to confirm **FL30**'s efficacy and safety profile. Further pharmacokinetic and pharmacodynamic studies will be necessary to determine optimal administration routes and dosing schedules. These steps will be critical for assessing **FL30**'s potential to progress toward clinical trials and

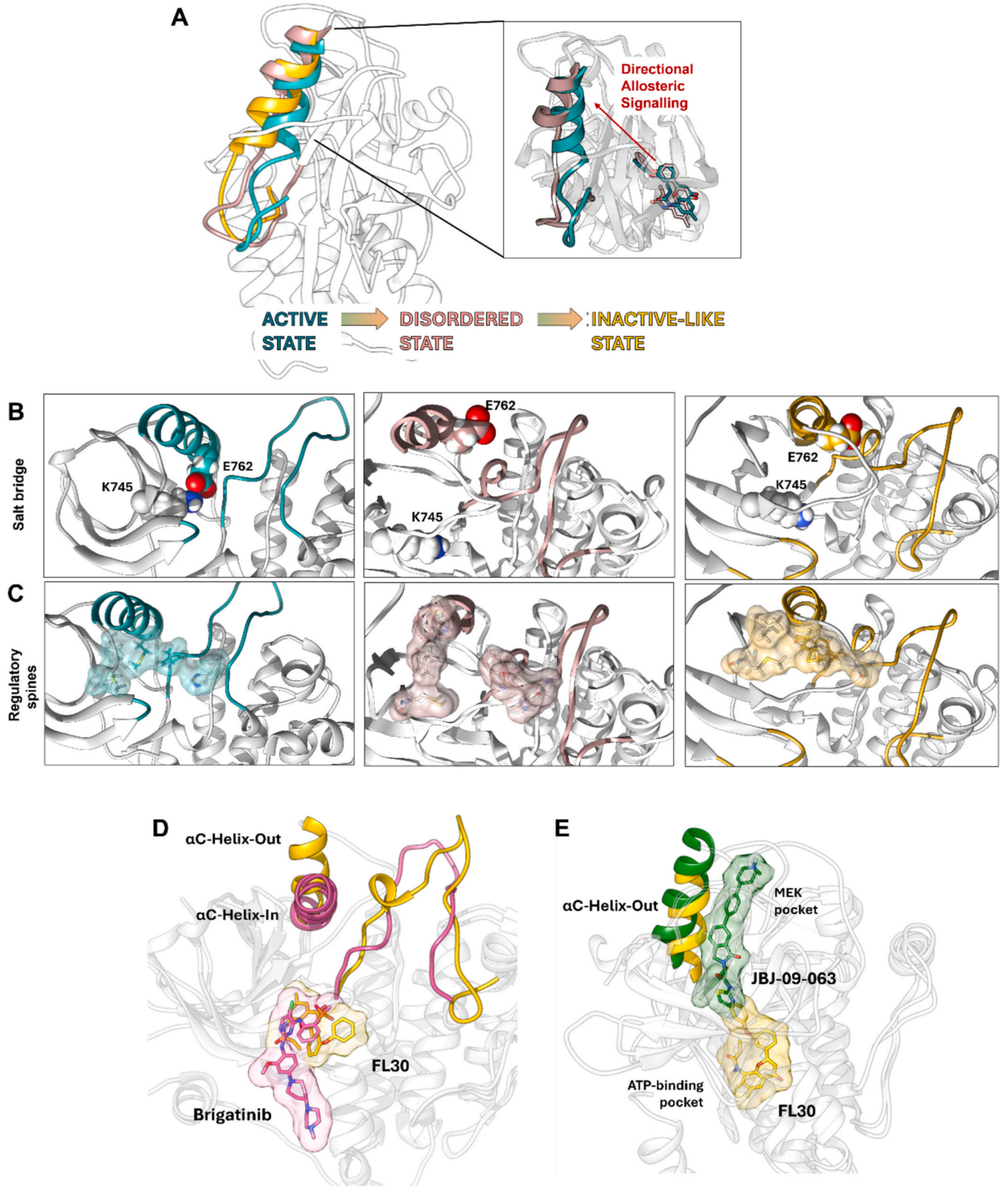

Fig. 5. **(A)** Representative structures of the EGFR-LT-FL30 derived from molecular dynamics simulation after 0.2 μs (rosy-brown) and 1 μs (gold) overlapped to the EGFR-LT in its active conformation. **(B)** Differences in the orientation of the K745 and E762, showed as spheres, which result in a different ability to promote the formation of the KE salt bridge, typical of the active EGFR conformation. **(C)** Conformation of the residues belonging to the regulatory spines residues shown as surface (M766, L777, M790, H835, P856): the linear conformation is one of the features of the active EGFR conformation while a distorted/disassembled conformation is typical of the inactive EGFR. **(D)** Crystal structure of EGFR-T790M/C797S in complex with Brigatinib (PDB: 7ZYM), with the compound, αC-helix, and A-loop highlighted in pink, overlapped with EGFR-L858R/T790M-FL30, in which the same regions are indicated in gold. **(E)** Crystal structure of EGFR-T790M/V948R in complex with the allosteric inhibitor JBJ-09-063 (PDB: 7JXQ), with the compound and αC-helix highlighted in forest green, overlapped with EGFR-L858R/T790M-FL30, in which the same regions are indicated in gold.

eventual therapeutic application, as well as for guiding structural modifications aimed at enhancing its efficacy and safety.

4. Experimental section

4.1. General methods and materials

All compounds used for the synthesis were purchased from Sigma Aldrich Co. (Stenheim, Germany) and used without purification. All solvents were analytically pure and dried before use. TLC were carried out on aluminum sheets precoated with silica gel 60 F254 (Merck). Column chromatography was performed using silica gel 60 (SiO_2, 230–400 mesh). High-resolution MS (HRMS) ESI and High-performance liquid chromatography-mass spectrometry (HPLC-MS) analyses were performed on Waters Xevo G2-XF QTof mass spectrometer. Mass spectrometric detection was performed in the positive ion mode for all compounds and in the negative ion mode. The ^{1}H and ^{13}C NMR spectra were recorded on the Agilent Technologies 400 MHz Premium Shielded, Bruker Ascend 500 Avance III HD and Bruker Ascend 600 avance NEO spectrometers. Chemical shifts (δ) are reported in ppm relative to TMS and coupling constants (J) in Hz.

4.2. Computational studies

4.2.1. Structural preparation of EGFR proteins and focused docking

The study used two distinct structural models: the inactive tyrosine kinase (TK) domain of the wild type (Wt) EGFR and the active TK domain of the EGFR variant L858R/T790M (designated as LT). They have been prepared starting from the PDB ID: 4HJO and 3W2O files, respectively as we previously described [11,28]. For the inactive wild type EGFR (Wt), we used the inactive EGFR form showing the key conformational features: the αC-helix-out conformation, the DFG-out position, the A-loop closed, and the R-spine with a linear conformation. In contrast, the active EGFR-LT variant was derived from molecular dynamics (MD) simulations conducted in our previous works which have been thoroughly validated and compared with PDB files [11,28]. In these studies, we monitored the conformational changes of the TK domain over time. Finally, EGFR-LT structure displayed a distinctly different set of conformational features than to inactive Wt EGFR: the αC-helix and DFG motif were in an "in" conformation, the A-loop was open, and the R-spine was distorted. These findings underscore the significant conformational differences between the inactive and active states of EGFR, which are critical to understanding its regulatory mechanisms.

The designed compounds have been generated starting from the flavone skeleton and adding the functional groups with UCSF Chimera. [55] All molecules have been then parametrized using quantum mechanical calculations based on Density Functional Theory (DFT) using hybrid functional B3LYP and 6-311G** basis set; the ligands' Mulliken charges have been calculated and included in the ligand input file for subsequent Focused Docking (FD) and Molecular Dynamics (MD) calculations. The implicit water GB/SA solvation method has been used to mimic the solvent effect. [56] The binding mode of each compound has been evaluated in the ATP-binding and allosteric pockets of wild type and EGFR-LT with a semiflexible docking approach using AutoDock Suite 4.2. [57] Since the binding pocket in EGFR-TK domains has been already described [58–60], and the starting structures as well as the final designed TKIs were small molecules with few rotational degrees of freedom, a focused grid field of 60 × 54 × 68 $Å^3$ has been generated centred on EGFR-TK pockets with points spaced equally at 0.375 Å intervals. The docking calculations have been carried out by AMBER-based empirical free energy force field as implemented in Autodock 4.2 combined with a Lamarckian Genetic Algorithm (LGA). The number of GA runs is settled to 100, while the maximum number of top individuals that automatically survive is 0.1. The resulting 100 docked conformations have been clustered into groups with similar binding modes by a root mean square deviation (RMSD) clustering tolerance of 2 Å to obtain a population percentage. The lowest energy conformations from the most populated clusters have been considered the most stable orientations. The sum of the intermolecular and the internal energies of the TKIs represents the docking energy, while the sum of the intermolecular and the torsional free energies is the free-binding energy. This calculated free binding energy can be related to the inhibition constant (Ki) through the known thermodynamic equation $\triangle G = -RT \ln Ki$. The most populated conformations and the resulting binding poses of each protein-drug complex have been deeply analyzed.

4.2.2. Molecular dynamics (MD) simulations

The docked complex of **FL30** in complex with EGFR-LT form underwent 1 μs of MD simulations using CHARMM36 force field. [61] The designed compounds were modelled and parametrized using quantum mechanical calculations based on Density Functional Theory (DFT), using the hybrid functional B3LYP and 6-311G** basis set to calculate the ligands' Mulliken charges and to compute a massive conformational analysis. [56] A simulation box of 120 $Å^3$ was settled for each complex including 54,867 TIP3P water molecules for solvation. Na^+ ions and Cl^- ions were also included to mimic the physiological conditions (0.15 M NaCl) and to neutralize the net charge of EGFR-TK. A minimization phase composed of 10,000 cycles of steepest descent followed by 5000 cycles of conjugate gradient minimization was used to converge to the energy threshold of 1000 KJ/mol/nm. The following equilibration step was adopted for each system to gradually accommodate the protein in the salt-aqueous environment. Verlet cutoff [62] was applied in combination with Particle Mesh Ewald (PME) for electrostatics. The cutoff for the calculation of the Van der Waals force was settled to 1.2 nm, while the force smoothly was switched to zero between 1.0 and 1.2 nm. Atom velocities were generated at 310 K in the NVT ensemble using the Maxwell distribution function with generated random seed and a weak temperature coupling using the Berendsen thermostat. A time constant of 1 ps was applied to maintain the reference temperature (310K) for the whole run. After equilibration simulation run of 2 ns, a switch to the NPT ensemble was carried out, maintaining the weak coupling also for pressure control (i.e., Berendsen barostat). For all simulation runs, the isotropic conditions were settled with a reference pressure of 1 atm and a time constant for coupling of 5 ps. A shift to the Nosé-Hoover [63] and Parrinello-Rahman algorithm for pressure coupling [64] was operated for the production phase in NPT Ensemble. Then, a 2 μs-long MD simulation was run for each system implementing an accurate leapfrog algorithm or interacting Newton's equations of motion with a time step of 0.002 ps. All the MD simulations were performed using GROMACS 5.0.4. [65,66] The 2D binding modes of small molecules obtained after MD simulations were detected using Discovery Studio, while the analysis of the simulations' trajectories was performed by means of the VMD [67] and CHIMERA software. [55]

4.3. Chemical synthesis

4.3.1. Synthesis of 1-(2-hydroxy-5-methoxy-3-nitrophenyl)ethenone (1b)

1-(2-Hydroxy-5-methoxyphenyl)ethenone (500 mg, 3 mmol, 1 eq) was suspended in Acetic acid (1 mL) and then Deionized water (300 μL) was added to the suspension. Nitric acid (265 μL, 6.4 mmol, 1.5 eq) was dripped into the mixture. The reaction was stirred at room temperature for 2 h. The product was extracted with ethyl acetate. The organic solvent was evaporated under reduced pressure and the crude was purified by silica gel column chromatography (R_f = 0.29, 25 % ethyl acetate in cyclohexane) to give compound **1b** as a yellow solid. Yield: 450 mg, 70.7 %. ^{1}H NMR (600 MHz, DMSO-d_6, 25 °C, ppm): δ 2.70 (s, 3H, CH_3), 3.84 (s, 3H, CH_3), 7.75 (d, J = 3.2 Hz, 1H, Ar—H), 7.80 (d, J = 3.2 Hz, 1H, Ar—H), 12.24 (s, 1H, OH). ^{13}C NMR (151 MHz, DMSO-d_6, 25 °C, ppm): δ 28.4, 56.4, 115.7, 122.4, 123.8, 138.1, 147.8, 150.4, 203.9. Calcd. neutral mass for $C_9H_9NO_5$: 211.04807 Da. HRMS: m/z = 210.04059 $[M-1]^-$.

4.3.2. (E)-1-(2-Hydroxy-5-methyl-3-nitrophenyl)-3-(3-phenoxyphenyl) prop-2-en-1-one (3a)

1-(2-Hydroxy-5-methyl-3-nitrophenyl)ethanone (**1a**) (1 g, 5.12 mmol, 1 eq) was dissolved in methanol and an aqueous solution of sodium hydroxide (840.5 mg, 41 mmol, 8 eq) was added. When all of **1a** was dissolved 3-phenoxybenzaldehyde (888 μL, 1 eq) could be added to the mixture. The reaction was stirred for 16 h at 45 °C, and then acidified to pH 5–6 by adding 5 % aqueous HCl. After extraction with EtOAc, the volatiles were removed under reduced pressure. The raw was purified by silica gel column chromatography (R_f = 0.31, 3 % ethyl acetate in cyclohexane) to afford the compound **3a** as a yellow solid. Yield: 798 mg, 41.5 %. ^{1}H NMR (400 MHz, DMSO-d_6, 25 °C, ppm): δ 2.35 (s, 3H, CH_3), 6.98–7.02 (m, 2H, Ar—H), 7.06 (ddd, *J* = 8.0, 2.5, 0.9 Hz, 1H, Ar—H), 7.10–7.15 (m, 1H, Ar—H), 7.33–7.42 (m, 2H, Ar—H), 7.46 (t, *J* = 8.0 Hz, 1H, Ar—H), 7.67–7.68 (m, 1H, Ar—H), 7.70–7.71 (m, 1H, Ar—H), 7.83 (d, *J* = 15.5 Hz, 1H, CH), 7.97 (d, *J* = 15.5 Hz, 1H, CH), 8.05 (d, *J* = 1.2 Hz, 1H, Ar—H), 8.39 (d, *J* = 1.2 Hz, 1H, Ar—H), 13.14 (s, 1H, OH). ^{13}C NMR (101 MHz, DMSO-d_6, 25 °C, ppm): δ 19.5, 118.3, 119.5, 121.5, 122.5, 123.3, 123.5, 125.1, 128.4, 130.1, 130.6, 131.0, 136.3, 136.5, 137.7, 145.5, 153.0, 156.6, 156.8, 193.4. Calcd. neutral mass for $C_{22}H_{17}NO_5$: 375,11,067 Da. Calcd. mass for $C_{22}H_{17}NO_5 + Na^+$: 398,09989 Da. HRMS: *m/z* = 376.11765 $[M + 1]^+$; 398.09942 $[M + Na]^+$.

4.3.3. (E)-1-(2-Hydroxy-5-methoxy-3-nitrophenyl)-3-(3-phenoxyphenyl) prop-2-en-1-one (3b)

1-(2-Hydroxy-5-methoxy-3-nitrophenyl)ethenone (**1b**) (450 mg, 2.1 mmol, 1 eq) was dissolved in methanol and a solution of potassium hydroxide (654.4 mg, 11.7 mmol, 5.5 eq) in methanol (2 mL) was added to the mixture. When all of **1b** was dissolved 3-phenoxybenzaldehyde (370 μL, 1 eq) could be added. The reaction was stirred for 24 h at 45 °C and then acidified to pH 5–6 by adding 5 % aqueous HCl. After extraction with EtOAc, the volatiles were removed under reduced pressure. The raw was purified by silica gel column chromatography (R_f = 0.28, 10 % ethyl acetate in cyclohexane) to afford the compound **3b** as a yellow solid. Yield: 200 mg, 24,4 %. ^{1}H NMR (600 MHz, DMSO-d_6, 25 °C, ppm): δ 3.87 (s, 3H, OCH_3), 7.04–7.06 (m, 2H, Ar—H), 7.10 (ddd, *J* = 8.1, 2.5, 0.9 Hz, 1H, Ar—H), 7.14–7.20 (m, 1H, Ar—H), 7.39–7.46 (m, 2H, Ar—H), 7.50 (t, *J* = 8.1 Hz, 1H, Ar—H), 7.70–7.71 (m, 1H, Ar—H), 7.72–7.74 (m, 1H, Ar—H), 7.80–7.86 (m, 2H, Ar—H, CH), 7.93 (d, *J* = 15.6 Hz, 1H, CH), 8.03 (d, *J* = 3.2 Hz, 1H, Ar—H), 12.46 (s, 1H, OH). ^{13}C NMR (151 MHz, DMSO-d_6, 25 °C, ppm): δ 56.5, 115.0, 118.3, 119.5, 121.5, 122.4, 123.4, 123.5, 125.0, 125.4, 130.1, 130.6, 136.4, 138.1, 145.5, 148.4, 150.6, 156.6, 156.9, 192.9. Calcd neutral mass for $C_{22}H_{17}NO_6$: 391,10,559 Da. HRMS: *m/z* = 392.11342 $[M + 1]^+$.

4.3.4. 6-Methyl-8-nitro-2-(3′-phenoxyphenyl)-4H-chromen-4-one (4a)

Iodine (42 mg, 0.17 mmol) was added to a solution of **3a** (420 mg, 1.12 mmol) in DMSO (8 mL) and the reaction mixture stirred at 130 °C for 6 h. After cooling to room temperature, the reaction was quenched with 0.5 % $NaHSO_3$ (aq) (50 mL). The mixture was extracted with CH_2Cl_2 (3 × 50 mL) and the combined organic layers washed with brine (100 mL) and dried over Na_2SO_4. Volatiles were removed under reduced pressure and the obtained residue was purified by silica gel column chromatography (R_f = 0.35, 20 % ethyl acetate in cyclohexane) to afford the compound **4a** as a white solid. Yield: 199 mg, 47.6 %. ^{1}H NMR (400 MHz, $CDCl_3$, 25 °C, ppm): δ 2.53 (s, 3H, CH_3), 6.81 (s, 1H, CH), 7.06 (dd, *J* = 8.7, 1.1 Hz, 2H, Ar—H), 7.15–7.20 (m, 2H, Ar—H), 7.35–7.42 (m, 2H, Ar—H), 7.48 (t, *J* = 8.0 Hz, 1H, Ar—H), 7.57 (t, *J* = 2.0 Hz, 1H, Ar—H), 7.72 (ddd, *J* = 7.9, 2.0, 1.0 Hz, 1H, Ar—H), 8.18 (d, *J* = 1.5 Hz, 1H, Ar—H), 8.28 (d, *J* = 1.5 Hz, 1H, Ar—H). ^{13}C NMR (101 MHz, $CDCl_3$, 25 °C, ppm): δ 20.8, 107.6, 116.0, 119.6, 121.1, 122.1, 124.3, 125.4, 130.1, 130.7, 130.8, 131.4, 132.3, 135.1, 138.3, 146.7, 156.1, 158.5, 163.0, 176.3. Calcd. neutral mass for $C_{22}H_{15}NO_5$: 373,09502 Da. HRMS: *m/z* = 374.10116 [M + 1] + .

4.3.5. 6-Methoxy-8-nitro-2-(3′-phenoxyphenyl)-4H-chromen-4-one (4b)

Iodine (18 mg, 0.07 mmol) was added to a solution of **3b** (180 mg, 0.46 mmol) in DMSO (8 mL) and the reaction mixture stirred at 130 °C for 6 h. After cooling to room temperature, the reaction was quenched with 0.5 % $NaHSO_3$ (aq) (50 mL). The mixture was extracted with CH_2Cl_2 (3 × 50 mL) and the combined organic layers were washed with brine (100 mL) and dried over Na_2SO_4. Volatiles were removed under reduced pressure and the obtained residue was purified by silica gel column chromatography (R_f = 0.28, 20 % ethyl acetate in cyclohexane) to afford the compound **4b** as a white solid. Yield: 113 mg, 63.1 %. ^{1}H NMR (600 MHz, DMSO-d_6, 25 °C, ppm): δ 3.96 (s, 3H, OCH_3), 7.07–7.13 (m, 2H, Ar—H), 7.18–7.25 (m, 3H, Ar—H, CH), 7.41–7.48 (m, 2H, Ar—H), 7.61 (t, *J* = 8.0 Hz, 1H, Ar—H), 7.76–7.80 (m, 2H, Ar—H), 7.89 (ddd, *J* = 8.0, 1.7, 0.8 Hz, 1H, Ar—H), 8.12 (d, *J* = 3.2 Hz, 1H, Ar—H). ^{13}C NMR (151 MHz, DMSO-d_6, 25 °C, ppm): δ 56.6, 106.9, 112.1, 116.4, 118.4, 118.9, 121.5, 121.9, 124.0, 125.8, 130.2, 131.0, 132.5, 139.1, 142.3, 155.1, 156.0, 157.4, 161.6, 175.3. Calcd. neutral mass for $C_{22}H_{15}NO_6$: 389,08994 Da. HRMS: *m/z* = 390.09790 $[M + 1]^+$.

4.3.6. 8-Amino-6-methyl-2-(3-phenoxyphenyl)-4H-chromen-4-one (5a)

The nitro group in compound **4a** was selective reduced using Palladium catalysis and H_2. Palladium on Carbon (Pd/C) (25 mg, 0.24 mmol) was added to the solution of **4a** (168 mg, 0.45 mmol) in CH_2Cl_2 (3 mL). The reaction was stirred at room temperature, under hydrogen atmosphere, for 24 h. After completion of the reaction, monitored by thin-layer chromatography (silica gel), the mixture of reaction was filtered with LLG-Plain disc filter. The volatiles of filtered were removed under reduced pressure and the obtained residue was purified by silica gel column chromatography (R_f = 0.39, 30 % ethyl acetate in cyclohexane) to afford the compound **5a** as a yellow solid. Yield: 78 mg, 50.5 %. ^{1}H NMR (400 MHz, DMSO-d_6, 25 °C, ppm): δ 2.29 (s, 3H, CH_3), 5.69 (s, 2H, NH_2), 6.89 (dd, *J* = 2.1, 0.7 Hz, 1H, Ar—H), 6.94 (s, 1H, CH), 6.99 (dd, *J* = 2.1, 0.9 Hz, 1H, Ar—H), 7.05–7.12 (m, 2H, Ar—H), 7.13–7.21 (m, 2H, Ar—H), 7.38–7.47 (m, 2H, Ar—H), 7.55 (t, *J* = 8.0 Hz, 1H, Ar—H), 7.94 (t, *J* = 2.0 Hz, 1H, Ar—H), 8.00 (ddd, *J* = 8.0, 2.0, 0.9 Hz, 1H, Ar—H). ^{13}C NMR (101 MHz, DMSO-d_6, 25 °C, ppm): δ 20.9, 106.9, 110.3, 117.2, 118.2, 118.7, 121.3, 121.8, 123.6, 123.7, 130.1, 130.7, 133.4, 134.8, 138.4, 142.5, 156.5, 157.1, 160.9, 177.5. Calcd. neutral mass for $C_{22}H_{17}NO_3$: 343,12,084 Da. HRMS: *m/z* = 344.12764 $[M + 1]^+$.

4.3.7. 8-Amino-6-methoxy-2-(3-phenoxyphenyl)-4H-chromen-4-one (5b)

The nitro group in compound **4b** was selectively reduced using Palladium catalysis and H_2. Palladium on Carbon (Pd/C) (17 mg, 0.16 mmol) was added at the solution of **4b** (113 mg, 0.29 mmol) in CH_2Cl_2 (3 mL). The reaction was stirred at room temperature, under hydrogen atmosphere, for 24 h. After completion of the reaction, monitored by thin-layer chromatography (silica gel), the mixture of reaction was filtered with LLG-Plain disc filter. The volatiles of filtered were removed under reduced pressure and the obtained residue was purified by silica gel column chromatography (R_f = 0.23, 30 % ethyl acetate in cyclohexane) to afford the compound **5b** as a yellow solid. Yield: 69 mg, 66.3 %. ^{1}H NMR (600 MHz, DMSO-d_6, 25 °C, ppm): δ 3.77 (s, 3H, OCH_3), 5.84 (s, 2H, NH_2), 6.64 (d, *J* = 3.0 Hz, 1H, Ar—H), 6.65 (d, *J* = 3.0 Hz, 1H, Ar—H), 6.97 (s, 1H, CH), 7.08 (dd, *J* = 8.6, 1.1 Hz, 2H, Ar—H), 7.15 (dd, *J* = 8.1, 1.9 Hz, 1H, Ar—H), 7.18 (tt, *J* = 7.4, 1.1 Hz, 1H, Ar—H), 7.43 (dd, *J* = 8.6, 7.4 Hz, 2H, Ar—H), 7.55 (t, *J* = 8.1 Hz, 1H, Ar—H), 7.96 (t, *J* = 1.9 Hz, 1H, Ar—H), 8.01 (ddd, *J* = 8.1, 1.9, 0.8 Hz, 1H, Ar—H). ^{13}C NMR (151 MHz, DMSO-d_6, 25 °C, ppm): δ 55.2, 91.4, 105.1, 106.4, 117.2, 118.6, 121.3, 121.8, 123.7, 124.4, 130.1, 130.7, 133.4, 139.9, 140.1, 156.5, 157.0, 157.1, 160.7, 177.3 Calcd. neutral mass for $C_{22}H_{17}NO_4$: 359,11,576 Da. HRMS: *m/z* = 360.12343 $[M + 1]^+$.

4.4. General procedure 1 for the synthesis of amide derivatives 6a-6e

The obtained amino derivatives (**5a-5b**) and 2 eq. (**6c, 6d**), 2.5 eq. (**6b, 6e**), 3 eq. (**6a**) of triethylamine were dissolved in CH_2Cl_2 (3 mL)

and cooled to 0 °C. The appropriate acyl chloride (**iiiia,** 1 eq; **iiiic,d** 1.2 eq; **iiiie,b** 1.5 eq) was added and the reaction was allowed to warm up to room temperature overnight. At the end the product was extracted by CH_2Cl_2 and then the volatiles were evapored under reduced pressure. The residue was purified by silica gel column chromatography with appropriate eluent mixture, to afford the final compound (**6a-e**).

4.4.1. N-(6-methyl-4-oxo-2-(3-phenoxyphenyl)-4H-chromen-8-yl) acrylamide (6a, FL30)

The synthesis was carried out in accordance with the general procedure **1**. The residue was purified by silica gel column chromatography ($R_f = 0.32$, 25 % ethyl acetate in cyclohexane) to give compound **6a** as a light-pink powder. Yield: 45 mg, 77.6 %. ^{1}H NMR (500 MHz, DMSO-d_6, 25 °C, ppm): δ 2.44 (s, 3H, CH_3), 5.80 (dd, $J = 10.2$, 1.9 Hz, 1H, CH_2), 6.28 (dd, $J = 17.1$, 1.9 Hz, 1H, CH_2), 6.52 (dd, $J = 17.1$, 10.2 Hz, 1H, CH), 7.06 (s, 1H, CH), 7.08 (d, $J = 7.5$ Hz, 2H, Ar—H), 7.18–7.22 (m, 2H, Ar—H), 7.41–7.46 (m, 2H, Ar—H), 7.58 (t, $J = 7.9$ Hz, 1H, Ar—H), 7.68 (d, $J = 2.2$ Hz, 1H, Ar—H), 7.83 (t, $J = 2.0$ Hz, 1H, Ar—H), 7.88 (d, $J = 2.2$ Hz, 1H, Ar—H), 7.91 (dd, $J = 7.9$, 2.0 Hz, 1H, Ar—H), 10.16 (s, 1H, NH). ^{13}C NMR (126 MHz, DMSO-d_6, 25 °C, ppm): δ 20.6, 107.4, 117.0, 118.6, 120.6, 121.8, 123.5, 123.7, 127.0, 127.4, 130.1, 130.1, 130.7, 131.1, 133.1, 134.6, 146.9, 156.3, 157.1, 161.3, 163.6, 176.8. Calcd. neutral mass of $C_{25}H_{19}NO_4$: 397,13,141 Da. HRMS: $m/z = 398.13812$ $[M + 1]^+$.

4.4.2. N-(6-methoxy-4-oxo-2-(3-phenoxyphenyl)-4H-chromen-8-yl) acrylamide (6b, FL31)

The synthesis was carried out in accordance with the general procedure **1**. The residue was purified by silica gel column chromatography ($R_f = 0.32$, 30 % ethyl acetate in cyclohexane) to give compound 6b as a yellow solid. Yield: 15 mg, 55.6 %. ^{1}H NMR (600 MHz, DMSO-d_6, 25 °C, ppm): δ 3.87 (s, 3H, CH_3), 5.82 (dd, $J = 10.2$, 1.8 Hz, 1H, CH_2), 6.29 (dd, $J = 17.0$, 1.8 Hz, 1H, CH_2), 6.53 (dd, $J = 17.0$, 10.2 Hz, 1H, CH), 7.07 (s, 1H, CH), 7.07–7.11 (m, 2H, Ar—H), 7.18 (tt, $J = 7.4$, 1.1 Hz, 1H, Ar—H), 7.21 (ddd, $J = 8.1$, 2.1, 0.9 Hz, 1H, Ar—H), 7.27 (d, $J = 3.1$ Hz, 1H, Ar—H), 7.39–7.46 (m, 2H, Ar—H), 7.58 (t, $J = 8.1$ Hz, 1H, Ar—H), 7.75 (d, $J = 3.1$ Hz, 1H, Ar—H), 7.78 (t, $J = 2.1$ Hz, 1H, Ar—H), 7.91 (ddd, $J = 8.1$, 2.1, 0.9 Hz, 1H, Ar—H), 10.20 (s, 1H, NH). ^{13}C NMR (151 MHz, DMSO-d_6, 25 °C, ppm): δ 55.8, 101.1, 106.9, 117.0, 117.4, 118.7, 121.8, 121.8, 123.8, 124.3, 127.9, 128.7, 130.2, 130.8, 131.1, 133.2, 143.4, 156.0, 156.3, 157.2, 161.3, 163.7, 176.6. Calcd. neutral mass of $C_{25}H_{19}NO_5$: 413.12632 Da. HRMS: $m/z = 414.13366$ $[M + 1]^+$.

4.4.3. N-(6-methyl-4-oxo-2-(3-phenoxyphenyl)-4H-chromen-8-yl) benzamide (6c, FL32)

The synthesis was carried out in accordance with the general procedure **1**. The residue was purified by silica gel column chromatography ($R_f = 0.33$, 20 % ethyl acetate in cyclohexane) to give compound **6c** as an orange solid. Yield: 41 mg, 54 %. ^{1}H NMR (400 MHz, DMSO-d_6, 25 °C, ppm): δ 2.43 (s, 3H, CH_3), 6.93–6.97 (m, 2H), 7.03 (s, 1H, CH), 7.07–7.12 (m, 1H, Ar—H), 7.12–7.15 (m, 1H, Ar—H), 7.29–7.35 (m, 2H, Ar—H), 7.43–7.51 (m, 3H, Ar—H), 7.54–7.60 (m, 1H, Ar—H), 7.71 (dd, $J = 2.2$, 1.0 Hz, 1H, Ar—H), 7.76–7.78 (m, 1H, Ar—H), 7.79 (d, $J = 2.2$ Hz, 1H, Ar—H), 7.80–7.83 (m, 1H, Ar—H), 7.97–7.98 (m, 2H, Ar—H), 10.40 (s, 1H, NH). ^{13}C NMR (101 MHz, DMSO-d_6, 25 °C, ppm): δ 20.6, 107.4, 117.5, 118.2, 121.3, 121.8, 122.0, 123.5, 123.7, 127.4, 127.6, 128.5, 130.1, 130.8, 131.7, 131.9, 133.4, 133.9, 134.7, 148.1, 156.6, 156.9, 161.3, 165.6, 176.9. Calcd. neutral mass for $C_{29}H_{21}NO_4$: 447.14706 Da. Calcd. mass for $C_{29}H_{21}NO_4 + Na^+$: 470,13,628 Da. HRMS: $m/z = 448.15377$ $[M + 1]^+$, 470.13607 $[M + Na]^+$.

4.4.4. N-(6-methyl-4-oxo-2-(3-phenoxyphenyl)-4H-chromen-8-yl) pivalamide (6d, FL33)

The synthesis was carried out in accordance with the general procedure **1**. The residue was purified by silica gel column chromatography ($R_f = 0.37$, 25 % ethyl acetate in cyclohexane) to give compound **6d** as an orange solid. Yield: 38 mg, 55.6 %. ^{1}H NMR (600 MHz, DMSO-d_6, 25 °C, ppm): δ 1.22 (s, 9H, CH_3), 2.43 (s, 3H, CH_3), 7.01–7.04 (m, 2H, Ar—H), 7.06 (s, 1H, CH), 7.16 (tt, $J = 7.4$, 1.1 Hz, 1H, Ar—H), 7.22 (ddd, $J = 8.0$, 2.1, 0.9 Hz, 1H, Ar—H), 7.39–7.43 (m, 2H, Ar—H), 7.59 (t, $J = 8.0$ Hz, 1H, Ar—H), 7.63 (d, $J = 2.2$ Hz, 1H, Ar—H), 7.69 (dd, $J = 2.2$, 1.0 Hz, 1H, Ar—H), 7.80 (t, $J = 2.1$ Hz, 1H, Ar—H), 7.89 (ddd, $J = 7.9$, 2.1, 0.9 Hz, 1H, Ar—H), 9.43 (s, 1H, NH). ^{13}C NMR (151 MHz, DMSO-d_6, 25 °C, ppm): δ 20.5, 27.2, 38.8, 107.3, 117.5, 118.1, 120.9, 122.0, 122.3, 123.5, 123.6, 127.6, 130.1, 130.8, 131.8, 133.5, 134.5, 148.0, 156.8, 156.8, 161.2, 176.6, 177.0. Calcd. neutral mass for $C_{27}H_{25}NO_4$: 427.17836 Da. Calcd mass for $C_{27}H_{25}NO_4 + Na^+$: 450,16,758 Da. HRMS: $m/z = 428.11638$ $[M + 1]^+$; 450.16888 $[M + Na]^+$.

4.4.5. N-(6-methyl-4-oxo-2-(3-phenoxyphenyl)-4H-chromen-8-yl) propionamide (6e, FL34)

The synthesis was carried out in accordance with the general procedure **1**. The residue was purified by silica gel column chromatography ($R_f = 0.3$, 25 % ethyl acetate in cyclohexane) to give compound **6e** as a pale yellow solid. Yield: 10 mg, 62.5 %. ^{1}H NMR (600 MHz, DMSO-d_6, 25 °C, ppm): δ 1.08 (t, $J = 7.5$ Hz, 3H, CH_3), 2.32 (q, $J = 7.5$ Hz, 2H, CH_2), 2.41 (s, 3H, CH_3), 7.06 (s, 1H, CH), 7.06–7.09 (m, 2H, Ar—H), 7.16–7.20 (m, 1H, Ar—H), 7.22 (dd, $J = 7.8$, 1.5 Hz, 1H, Ar—H), 7.59 (t, $J = 7.8$ Hz, 1H, Ar—H), 7.65 (d, $J = 2.5$ Hz, 1H, Ar—H), 7.75 (d, $J = 2.5$ Hz, 1H, Ar—H), 7.83 (t, $J = 1.5$ Hz, 1H, Ar—H), 7.92 (dd, $J = 7.8$, 1.5 Hz, 1H, Ar—H), 9.88 (s, 1H, NH). ^{13}C NMR (151 MHz, DMSO-d_6, 25 °C, ppm): δ 9.7, 20.7, 29.1, 107.4, 117.1, 118.6, 120.4, 121.9, 122.0, 123.6, 123.7, 127.4, 130.2, 130.5, 130.9, 133.3, 134.6, 147.2, 156.5, 157.1, 161.3, 172.3, 177.0. Calcd. neutral mass of $C_{25}H_{21}NO_4$: 399,14,706 Da. Calcd. mass for $C_{25}H_{21}NO_4 + Na^+$: 422,13,628 Da. HRMS: $m/z = 400.15400$ $[M + 1]^+$, 422.13712 $[M + Na]^+$.

4.5. Cellular materials and methods

4.5.1. Cell culture

The human non-small cell lung cancer (NSCLC) cell line was all obtained from the American Type Culture Collection (ATCC). The H1975 (CRL-5908™) cell line was grown in RPMI 1640 medium (SIAL-RPMI-XA) while the A549 (CCL-185™, high-expressing wild type EGFR) was grown in complete DMEM medium (SIAL-DMEM-HPXA) as well as the breast cancer cells MCF7 (low-expressing EGFR wild type) and human dermal fibroblasts (HDF). All cultures were supplemented with 10 % fetal bovine serum (FBS), 2 mM L-glutamine, 100 U / mL penicillin, and 100 μg / mL streptomycin. All cell lines were routinely maintained in 75 cm^2 flasks in a cell incubator at 37 °C, 5 % CO_2, and 95 % relative humidity. The cell cultures were detached by trypsinization with 0.5 % trypsin in PBS containing 0.025 % EDTA. All cell culture reagents were supplied by SIAL (Roma, Italy).

4.5.2. XTT assay

Cell Proliferation Kit II (XTT) (Roche) was used according to the manufacturer's protocol. H1975, A549, HDF and MCF7 cells were seeded in 96-well plates at 3×10^5 cells/well to reach 60 % of confluence after 24 h. Then, 200 μL of compound at different concentrations were added to each well. After incubation of 72 h at 37 °C and 5 % CO_2, the supernatant was removed from each well and replaced with 100 μL of fresh complete medium. The mix containing labelling reagent and electron reagent was then prepared; 50 μL of this mix was added to each well and incubated for 4 h at 37 °C and 5 % CO_2. Reading was then carried out with the multiple reader at a wavelength of 450 nm.

4.5.3. EGFR phosphorylation studies by flow cytometry

A549 and H1975 were seeded in 25 cm^2 flasks to reach after 24 h 60 % confluence. For induction of EGFR phosphorylation, A549 cells were incubated for 10 min with 50 ng/mL recombinant EGF (Euroclone), before **FL30** treatment for 4 and 24 h. After incubation, cells were washed with PBS buffer (pH, 7.4) containing sodium orthovanadate

Na_3VO_4 and (1 mM) sodium fluoride NaF (1 mM) to inhibit the phosphatase activity. Cells were then detached by trypsinization and prepared for the specific analyses. Cells were prepared following the previously described protocol [68] which consist of cell fixation (2 % paraformaldehyde), permeabilization for 30 min on ice in PBS, 0.5 % BSA and 0.025 % Triton X100 and antibodies staining with EGFR (Invitrogen, MA5–28104) and phospho-EGFR (Y1068) (R&D System, IC3570F). After incubation for 1 h in the dark at 4 °C, at least 5000 cells for each sample were measured using the same settings. For inhibiting potential phosphatase activity, the staining and permeabilization buffers were supplemented with NaF and Na_3VO_4 to a final concentration of 1 mM. The percentage of EGFR phosphorylation was calculated by dividing the geometric mean fluorescence intensity of phospho-EGFR by the geometric mean fluorescence intensity of the EGFR.

4.6. Enzyme inhibition assays

We used a continuous, fluorescence-based assay based on PhosphoSens technology (Assay Quant) to assess the protein kinase activity and inhibition. Recombinant wild-type (Wt) and L858R/T790M EGFR kinase domains were produced according to [44]. Briefly, His-tagged proteins were expressed in Sf9 cells and purified using immobilized metal affinity chromatography (IMAC), anion exchange, and size-exclusion chromatography. Purified proteins were stored at −80 °C in a buffer containing 25 mM Hepes (pH 8), 250 mM NaCl, 5 % glycerol, and 2 mM TCEP. L858R/T790M/C797S EGFR kinase domain was purchased from Merck (PRECISIO ®Kinase, recombinant SRP0710). Kinase activities for mutants (L858R/T790M and L858R/T790M/C797S) and Wild type EGFR were performed at 30 °C with 0.1 μM enzyme, 10 μM peptide substrate AQT0734 (Assay Quant) and 1 mM ATP. For the preliminary screening, synthesized TKIs were tested at a single dose of 1 μM, while for the IC_{50} determinations inhibitor concentrations ranged from 0.03 μM to 10 μM. The total assay reaction volume was 25 μL and included 50 mM HEPES, 20 mM NaCl, 10 mM $MgCl_2$, 0.1 mg/mL BSA, 1 % DMSO, and 2 mM DTT, adjusted to pH 7.5. Assay components were dispensed into a 384-well assay microplate (Corning 3572). Reactions were initiated by the addition of ATP following a 5-min preincubation period. The accumulation of the phosphorylated peptide product was monitored using a Synergy HT plate reader (Biotek) equipped with a fluorescence intensity module with excitation at 360 nm and emission at 480 nm for 1 h. For the time-dependant inhibition test, the pre-incubation period was extended to 45 min. Kinase selectivity assay on a panel of ten kinases (JNK2, BTK, ERK2, FGFR4, AKT1, ALK, ALK C1156Y, CDK2, and MET) were performed at Kinase Screening Assay Services (Reaction Biology Europe GmbH, Engesserstr. 479,108 Freiburg, GERMANY, https://www.reactionbiology.com/services/kinase-assays/kinase-panel-screening/) by using radiometric protein kinase assay (^{33}PanQinase™ Activity Assay) and by using different ATP concentrations, corresponding to the apparent ATP-K_m of the respective kinase,

4.7. SEIRA spectroscopy

Surface Enhanced InfraRed Absorption Spectroscopy (SEIRA) is plasmon-assisted spectroscopic technique that allows for the detection and measurement of analytes in small concentrations or in small amount when they can be placed in proximity to with the plasmonic structures. These molecules can be anchored directly onto the resonant structures prior the measurements and it is possible to observe the interaction of these molecules with those in solution, if any.

For the experiments here reported, golden crossed-shaped nano-antennas arrays were fabricated on calcium fluoride substrates as in Zucchiatti et at. 2021 [44]. Measurements were carried out in ATR-like configuration, with the incoming IR light illuminating the backside of the structures, generating an evanescent field that interacts with the in house produced proteins (see previous paragraph) anchored via His-tag. The reflected light then is sent to the detector obtaining a spectrum. The measure configuration is known as Plasmonic Internal Reflection (PIR) [69]. The CaF_2 window with the plasmonic structures is placed into a liquid chamber containing either buffer, or buffer plus **FL30** (0.1 μM) or **FL4** (10 μM). Data were acquired at the SISSI-Bio Beamline at Elettra [70] using a Hyperion 3000 Vis/IR microscope coupled with the in-vacuum Vertex 70v interferometer (Bruker Optics, Billerica, MA, US). Each spectrum was collected with and MCT (mercury cadmium telluride, Infrared Associates Inc., Stuart, FL, US) detector, averaging 256 scans at 4 cm^{-1}, setting the apertures of the microscope at 50 × 50 μmˆ2, in order to match the size of a single nano-antenna array. Each plasmonic chip contains 16 independent nano-antennas arrays, therefore each measurement is similar to operate in a16 well-plate. In addition, all experiments have been carried out at least twice on different plasmonic chips. Data were collected using OPUS software (Bruker Optics, Billerica, MA, US) and then analyzed using QUASAR 1.10 [71,72] (https:\\quasar.codes) and Origin 2024 Pro. [73]

CRediT authorship contribution statement

Elena Romagnoli: Investigation, Data curation, Writing – review & editing, Methodology, Conceptualization. **Emiliano Laudadio:** Conceptualization, Software, Writing – review & editing, Methodology, Data curation, Writing – original draft, Formal analysis. **Giovanna Mobbili:** Visualization, Conceptualization, Writing – review & editing, Data curation. **Leonardo Sorci:** Formal analysis, Investigation, Data curation, Methodology. **Giovanni Birarda:** Writing – original draft, Formal analysis, Methodology, Conceptualization, Investigation, Data curation. **Federica Piccirilli:** Data curation, Methodology. **Lisa Vaccari:** Data curation, Writing – review & editing, Methodology, Formal analysis. **Hendrik Vondracek:** Methodology. **Brenda Romaldi:** Methodology. **Massimo Marcaccio:** Methodology. **Paola Storici:** Resources, Data curation, Formal analysis, Methodology. **Marta Semrau:** Formal analysis, Methodology, Data curation. **Roberta Galeazzi:** Writing – review & editing, Methodology, Formal analysis. **Andrea Toma:** Data curation, Methodology, Writing – review & editing, Resources. **Vincenzo Aglieri:** Methodology, Formal analysis. **Pierluigi Stipa:** Resources. **Tatiana Armeni:** Methodology. **Cristina Minnelli:** Writing – review & editing, Project administration, Formal analysis, Writing – original draft, Resources, Data curation, Funding acquisition, Supervision, Conceptualization.

Declaration of competing interest

The authors declare the following financial interests/personal relationships which may be considered as potential competing interests: Minnelli Cristina reports financial support was provided by Airc Italian Foundation for Cancer Research. If there are other authors, they declare that they have no known competing financial interests or personal relationships that could have appeared to influence the work reported in this paper.

Acknowledgements

This work was supported by FIRC-AIRC (Fondazione Italiana per la Ricerca Sul Cancro), providing a postdoctoral research grant No. 25234 (two years fellowship) for the year 2021–2022 (C.M.). F.P. and M.S.S. research activities were supported by the European Union – NextGenerationEU within the project PNRR"PRP@CERIC" IR0000028 - Mission 4 Component 2 Investment 3.1 Action 3.1.1. The authors would like to acknowledge CINECA-HPC ISCRA MARCONI-100 computer system (ATOM-HMV project n. HP10CRO8W4) for the calculations on GROMACS and Elettra beamline SISSI-Chem - Life Sci (project n. 20210191).

Appendix A. Supplementary data

Supplementary data to this article can be found online at https://doi.org/10.1016/j.ijbiomac.2025.145453.

References

[1] E. Laudadio, L. Mangano, C. Minnelli, Chemical scaffolds for the clinical development of mutant-selective and reversible fourth-generation EGFR-TKIs in NSCLC, ACS Chem. Biol. 19 (2024) 839–854, https://doi.org/10.1021/acschembio.4c00028.

[2] J. Engel, C. Becker, J. Lategahn, M. Keul, J. Ketzer, T. Mühlenberg, et al., Inhibition wirkstoffresistenter Mutationsvarianten der Rezeptortyrosinkinase EGFR, Angew. Chem. 128 (2016) 11069–11073, https://doi.org/10.1002/ange.201605011.

[3] T. Damghani, F. Wittlinger, T.S. Beyett, M.J. Eck, S.A. Laufer, D.E. Heppner, Structural elements that enable specificity for mutant EGFR kinase domains with next-generation small-molecule inhibitors, Methods Enzymol. 685 (2023) 171–198, https://doi.org/10.1016/BS.MIE.2023.03.013.

[4] C. Minnelli, E. Laudadio, L. Sorci, G. Sabbatini, R. Galeazzi, A. Amici, et al., Identification of a novel nitroflavone-based scaffold for designing mutant-selective EGFR tyrosine kinase inhibitors targeting T790M and C797S resistance in advanced NSCLC, Bioorg. Chem. (2022) 129, https://doi.org/10.1016/j.bioorg.2022.106219.

[5] S. Park, B.M. Ku, H.A. Jung, J.M. Sun, J.S. Ahn, S.H. Lee, et al., EGFR C797S as a resistance mechanism of lazertinib in non-small cell lung cancer with EGFR T790M mutation, Cancer Res. Treat. 52 (2020) 1288–1290, https://doi.org/10.4143/crt.2020.278.

[7] R. Roskoski, Classification of small molecule protein kinase inhibitors based upon the structures of their drug-enzyme complexes, Pharmacol. Res. 103 (2016) 26–48, https://doi.org/10.1016/j.phrs.2015.10.021.

[8] Z. Zhao, P.E. Bourne, Progress with covalent small-molecule kinase inhibitors, Drug Discov. Today 23 (2018) 727–735, https://doi.org/10.1016/j.drudis.2018.01.035.

[9] S. Panjarian, R.E. Iacob, S. Chen, J.R. Engen, Structure and dynamic regulation of Abl kinases, J. Biol. Chem. 288 (2013) 5443–5450, https://doi.org/10.1074/jbc.R112.438382.

[10] O.P.J. Van Linden, A.J. Kooistra, R. Leurs, I.J.P. De Esch, C. De Graaf, KLIFS: a knowledge-based structural database to navigate kinase-ligand interaction space, J. Med. Chem. 57 (2014) 249–277, https://doi.org/10.1021/jm400378w.

[11] E. Laudadio, F. Piccirilli, H. Vondracek, G. Mobbili, M.S. Semrau, P. Storici, R. Galeazzi, E. Romagnoli, L. Sorci, A. Toma, V. Aglieri, G. Birarda, C. Minnelli, Probing conformational dynamics of EGFR mutants via SEIRA spectroscopy: potential implications for tyrosine kinase inhibitor design, Phys. Chem. Chem. Phys. 26 (2024) 22853–22857, https://doi.org/10.1039/D4CP02232G.

[12] C.-H. Yun, K.E. Mengwasser, A.V. Toms, M.S. Woo, H. Greulich, K.-K. Wong, et al., The T790M Mutation in EGFR Kinase Causes Drug Resistance by Increasing the Affinity for ATP, Proc. Natl. Acad. Sci. USA 105 (2008) 2070–2075, https://doi.org/10.1073/pnas.0709662105.

[13] J.R. Simard, S. Klüter, C. Grütter, M. Getlik, M. Rabiller, H.B. Rode, et al., A new screening assay for allosteric inhibitors of cSrc, Nat. Chem. Biol. 5 (2009) 394–396, https://doi.org/10.1038/nchembio.162.

[14] Y. Jia, C.H. Yun, E. Park, D. Ercan, M. Manuia, J. Juarez, et al., Overcoming EGFR (T790M) and EGFR(C797S) resistance with mutant-selective allosteric inhibitors, Nature 534 (2016) 129–132, https://doi.org/10.1038/nature17960.

[15] J.M. Baas, L.L. Krens, H.J. Guchelaar, J. Ouwerkerk, F.A. de Jong, A.P.M. Lavrijsen, et al., Recommendations on management of EGFR inhibitor-induced skin toxicity: a systematic review, Cancer Treat. Rev. 38 (2012) 505–514, https://doi.org/10.1016/j.ctrv.2011.09.004.

[16] C. To, J. Jang, T. Chen, E. Park, M. Mushajiang, D.J.H. De Clercq, et al., Single and dual targeting of mutant egfr with an allosteric inhibitor, Cancer Discov. 9 (2019) 926–943, https://doi.org/10.1158/2159-8290.CD-18-0903.

[17] To C, T.S. Beyett, J. Jang, W.W. Feng, M. Bahcall, H.M. Haikala, et al., An allosteric inhibitor against the therapy-resistant mutant forms of EGFR in non-small cell lung cancer, Nat. Can. 3 (2022) 402–417, https://doi.org/10.1038/s43018-022-00351-8.

[18] E. Michael, D.A. Scott, J. Pasi, S. Beyett Tyler, J. Jie, G. Praful, et al., EAI-432: A Mutant-Selective Allosteric EGFR Inhibitor for L858R-Mutant Non-small Cell Lung cancer, Boston, MA, Philadelphia (PA), in: Proceedings of the AACR-NCI-EORTC Virtual International Conference on Molecular Targets and Cancer Therapeutics, 2023.

[19] Q. Li, T. Zhang, S. Li, L. Tong, J. Li, Z. Su, et al., Discovery of potent and noncovalent reversible EGFR kinase inhibitors of EGFRL858R/T790M/C797S, ACS Med. Chem. Lett. 10 (2019) 869–873, https://doi.org/10.1021/acsmedchemlett.8b00564.

[20] F. Wittlinger, B.C. Ogboo, E. Shevchenko, T. Damghani, C.D. Pham, I.K. Schaeffner, et al., Linking ATP and allosteric sites to achieve superadditive binding with bivalent EGFR kinase inhibitors, Commun Chem (2024) 7, https://doi.org/10.1038/s42004-024-01108-3.

[21] F. Wittlinger, D.E. Heppner, To C, M. Günther, B.H. Shin, J.K. Rana, et al., Design of a "two-in-one" mutant-selective epidermal growth factor receptor inhibitor that spans the Orthosteric and allosteric sites, J. Med. Chem. 65 (2022) 1370–1383, https://doi.org/10.1021/acs.jmedchem.1c00848.

[22] S. Sogabe, Y. Kawakita, S. Igaki, H. Iwata, H. Miki, D.R. Cary, et al., Structure-based approach for the discovery of pyrrolo[3,2- d]pyrimidine-based EGFR T790M/L858R mutant inhibitors, ACS Med. Chem. Lett. 4 (2013) 201–205, https://doi.org/10.1021/ml300327z.

[23] A. Wang, X. Li, H. Wu, F. Zou, X.E. Yan, C. Chen, et al., Discovery of (R)-1-(3-(4-Amino-3-(3-chloro-4-(pyridin-2-ylmethoxy)phenyl)-1H-pyrazolo[3,4-d]pyrimidin-1-yl)piperidin-1-yl)prop-2-en-1-one (CHMFL-EGFR-202) as a novel irreversible EGFR mutant kinase inhibitor with a distinct binding mode, J. Med. Chem. 60 (2017) 2944–2962, https://doi.org/10.1021/acs.jmedchem.6b01907.

[24] Y.H. Peng, H.Y. Shiao, C.H. Tu, P.M. Liu, J.T.A. Hsu, P.K. Amancha, et al., Protein kinase inhibitor design by targeting the asp-Phe-Gly (DFG) motif: the role of the DFG motif in the design of epidermal growth factor receptor inhibitors, J. Med. Chem. 56 (2013) 3889–3903, https://doi.org/10.1021/jm400072p.

[25] Y. Qiu, X. Yin, X. Li, Y. Wang, Q. Fu, R. Huang, et al., Untangling dual-targeting therapeutic mechanism of epidermal growth factor receptor (Egfr) based on reversed allosteric communication, Pharmaceutics (2021) 13, https://doi.org/10.3390/pharmaceutics13050747.

[26] S. Du, J.J. Alvarado, T.E. Wales, J.A. Moroco, J.R. Engen, T.E. Smithgall, ATP-site inhibitors induce unique conformations of the acute myeloid leukemia-associated Src-family kinase, Fgr. Structure 30 (2022) 1508–1517.e3, https://doi.org/10.1016/j.str.2022.08.008.

[27] P. Pan, H. Yu, Q. Liu, X. Kong, H. Chen, J. Chen, et al., Combating drug-resistant mutants of anaplastic lymphoma kinase with potent and selective type-II1/2 inhibitors by stabilizing unique DFG-shifted loop conformation, ACS Cent. Sci. 3 (2017) 1208–1220, https://doi.org/10.1021/acscentsci.7b00419.

[28] E. Laudadio, G. Mobbili, L. Sorci, R. Galeazzi, C. Minnelli, Mechanistic insight toward EGFR activation induced by ATP: role of mutations and water in ATP binding patterns, J. Biomol. Struct. Dyn. 41 (2023) 6492–6501, https://doi.org/10.1080/07391102.2022.2108497.

[29] D.E. Heppner, M. Günther, F. Wittlinger, S.A. Laufer, M.J. Eck, Structural basis for EGFR mutant inhibition by Trisubstituted imidazole inhibitors, J. Med. Chem. 63 (2020) 4293–4305, https://doi.org/10.1021/acs.jmedchem.0c00200.

[30] T.S. Beyett, J.K. Rana, I.K. Schaeffner, D.E. Heppner, M.J. Eck, Structural analysis of the macrocyclic inhibitor BI-4020 binding to EGFR kinase, Chem. Med. Chem. (2024) 19, https://doi.org/10.1002/cmdc.202300343.

[31] C. Minnelli, E. Laudadio, L. Sorci, G. Sabbatini, R. Galeazzi, A. Amici, et al., Identification of a novel nitroflavone-based scaffold for designing mutant-selective EGFR tyrosine kinase inhibitors targeting T790M and C797S resistance in advanced NSCLC, Bioorg. Chem. (2022) 129, https://doi.org/10.1016/j.bioorg.2022.106219.

[32] H. Zhou, H. Fu, X. Shao, W. Cai, Binding thermodynamics of fourth-generation EGFR inhibitors revealed by absolute binding free energy calculations, J. Chem. Inf. Model. 63 (2023) 7837–7846, https://doi.org/10.1021/acs.jcim.3c01636.

[33] H. Park, H.Y. Jung, S. Mah, S. Hong, Discovery of EGF receptor inhibitors that are selective for the d746-750/T790M/C797S mutant through structure-based de novo design, Angew. Chem. Int. Ed. 56 (2017) 7634–7638, https://doi.org/10.1002/anie.201703389.

[34] Y. Zuo, Z. Long, R. Li, Y. Le, S. Zhang, H. He, et al., Design, synthesis and antitumor activity of 4-arylamine substituted pyrimidine derivatives as noncovalent EGFR inhibitors overcoming C797S mutation, Eur. J. Med. Chem. (2024) 265, https://doi.org/10.1016/j.ejmech.2023.116106.

[35] S.M. Lim, T. Fujino, C. Kim, G. Lee, Y.H. Lee, D.W. Kim, et al., BBT-176, a novel fourth-generation tyrosine kinase inhibitor for osimertinib-resistant egfr mutations in non–small cell lung cancer, Clin. Cancer Res. 29 (2023) 3004–3016, https://doi.org/10.1158/1078-0432.CCR-22-3901.

[36] S. Ding, Z. Gao, Z. Hu, R. Qi, X. Zheng, X. Dong, et al., Design, synthesis and biological evaluation of novel osimertinib derivatives as reversible EGFR kinase inhibitors, Eur. J. Med. Chem. (2022) 238, https://doi.org/10.1016/j.ejmech.2022.114492.

[37] A. Thorarensen, P. Balbo, M.E. Banker, R.M. Czerwinski, M. Kuhn, T.S. Maurer, et al., The advantages of describing covalent inhibitor in vitro potencies by IC50 at a fixed time point. IC50 determination of covalent inhibitors provides meaningful data to medicinal chemistry for SAR optimization, Bioorg. Med. Chem. (2021) 29, https://doi.org/10.1016/j.bmc.2020.115865.

[38] T. Zhang, F. Inesta-Vaquera, M. Niepel, J. Zhang, S.B. Ficarro, T. MacHleidt, et al., Discovery of potent and selective covalent inhibitors of JNK, Chem. Biol. 19 (2012) 140–154, https://doi.org/10.1016/j.chembiol.2011.11.010.

[39] I. Aronchik, Y. Dai, M. Labenski, C. Barnes, T. Jones, L. Qiao, et al., Efficacy of a covalent ERK1/2 inhibitor, CC-90003, in KRAS-mutant Cancer models reveals novel mechanisms of response and resistance, Mol. Cancer Res. 17 (2019) 642–654, https://doi.org/10.1158/1541-7786.MCR-17-0554.

[40] L.A. Honigberg, A.M. Smith, M. Sirisawad, E. Verner, D. Loury, B. Chang, et al., The Bruton tyrosine kinase inhibitor PCI-32765 blocks B-cell activation and is efficacious in models of autoimmune disease and B-cell malignancy, Proc. Natl. Acad. Sci. USA 107 (2010) 13075–13080, https://doi.org/10.1073/pnas.1004594107.

[41] L. van der Westhuizen, J. Weisner, A. Taher, I. Landel, L. Quambusch, M. Lindemann, et al., Covalent allosteric inhibitors of Akt generated using a click fragment approach, Chem. Med. Chem. (2022) 17, https://doi.org/10.1002/cmdc.202100776.

[42] X. Chen, Y. Huang, B. Chen, H. Liu, Y. Cai, Y. Yang, Insight into the design of FGFR4 selective inhibitors in cancer therapy: prospects and challenges, Eur. J. Med. Chem. (2024) 263, https://doi.org/10.1016/j.ejmech.2023.115947.

[43] F. Wittlinger, B.C. Ogboo, E. Shevchenko, T. Damghani, C.D. Pham, I.K. Schaeffner, et al., Linking ATP and allosteric sites to achieve superadditive binding with bivalent EGFR kinase inhibitors, Commun. Chem. (2024) 7, https://doi.org/10.1038/s42004-024-01108-3.

[44] P. Zucchiatti, G. Birarda, A. Cerea, M.S. Semrau, A. Hubarevich, P. Storici, et al., Binding of tyrosine kinase inhibitor to epidermal growth factor receptor: surface-enhanced infrared absorption microscopy reveals subtle protein secondary structure variations, Nanoscale 13 (2021) 7667–7677, https://doi.org/10.1039/d0nr09200b.
[45] R. Adato, H. Altug, In-situ ultra-sensitive infrared absorption spectroscopy of biomolecule interactions in real time with plasmonic nanoantennas, Nat. Commun. (2013) 4, https://doi.org/10.1038/ncomms3154.
[46] F. Piccirilli, H. Vondracek, L. Silvestrini, P. Parisse, F. Spinozzi, L. Vaccari, et al., Dimeric and monomeric conformation of SARS-CoV-2 main protease: new technical approaches based on IR radiation, Spectrochim. Acta A Mol. Biomol. Spectrosc. 322 (2024), https://doi.org/10.1016/j.saa.2024.124772.
[47] E.R. Wood, A.T. Truesdale, O.B. Mcdonald, D. Yuan, A. Hassell, S.H. Dickerson, et al., A Unique Structure for Epidermal Growth Factor Receptor Bound to GW572016 (Lapatinib): Relationships among Protein Conformation, Inhibitor Off-Rate, and Receptor Activity in Tumor Cells 64, 2004, https://doi.org/10.1158/0008-5472.CAN-04-1168.
[48] J. Kong, S. Yu, Fourier transform infrared spectroscopic analysis of protein secondary structures, Acta Biochim. Biophys. Sin. Shanghai 39 (2007) 549–559, https://doi.org/10.1111/j.1745-7270.2007.00320.x.
[49] A. Adochitei, G. Drochioiu, Rapid Characterization of peptide secondary structure by FT-IT spectroscopy, Rev. Roum. Chim. 56 (2011) 783–791.
[50] B.R. Singh, Infrared Analysis of Peptides and Proteins : Principles and Applications, American Chemical Society, 2000.
[51] H. Yang, S. Yang, J. Kong, A. Dong, S. Yu, Obtaining information about protein secondary structures in aqueous solution using Fourier transform IR spectroscopy, Nat. Protoc. 10 (2015) 382–396, https://doi.org/10.1038/nprot.2015.024.
[52] A. Barth, The infrared absorption of amino acid side chains, Prog. Biophys. Mol. Biol. 74 (2000) 141–173, https://doi.org/10.1016/s0079-6107(00)00021-3.
[53] Y. Shan, A. Arkhipov, E.T. Kim, A.C. Pan, D.E. Shawa, Transitions to catalytically inactive conformations in EGFR kinase, Proc. Natl. Acad. Sci. USA 110 (2013) 7270–7275, https://doi.org/10.1073/pnas.1220843110.
[54] Y. Shan, M.P. Eastwood, X. Zhang, E.T. Kim, A. Arkhipov, R.O. Dror, et al., Oncogenic mutations counteract intrinsic disorder in the EGFR kinase and promote receptor dimerization, Cell 149 (2012) 860–870, https://doi.org/10.1016/j.cell.2012.02.063.
[55] E.F. Pettersen, T.D. Goddard, C.C. Huang, G.S. Couch, D.M. Greenblatt, E.C. Meng, et al., UCSF Chimera - a visualization system for exploratory research and analysis, J. Comput. Chem. 25 (2004) 1605–1612, https://doi.org/10.1002/jcc.20084.
[56] A.V. Onufriev, G. Sigalov, A strategy for reducing gross errors in the generalized born models of implicit solvation, J. Chem. Phys. (2011) 134, https://doi.org/10.1063/1.3578686.
[57] G.M. Morris, H. Ruth, W. Lindstrom, M.F. Sanner, R.K. Belew, D.S. Goodsell, et al., Software news and updates AutoDock4 and AutoDockTools4: automated docking with selective receptor flexibility, J. Comput. Chem. 30 (2009) 2785–2791, https://doi.org/10.1002/jcc.21256.
[58] Z. Zhao, L. Xie, P.E. Bourne, Structural Insights into Characterizing Binding Sites in Epidermal Growth Factor Receptor Kinase Mutants, J. Chem. Inf. Model. 62 (2022) 223–224, https://doi.org/10.1021/acs.jcim.1c01357.
[59] C. Minnelli, E. Laudadio, G. Mobbili, R. Galeazzi, Conformational insight on WT- and mutated-EGFR receptor activation and inhibition by epigallocatechin-3-gallate: over a rational basis for the design of selective non-small-cell lung anticancer agents, Int. J. Mol. Sci. (2020) 21, https://doi.org/10.3390/ijms21051721.
[60] E. Laudadio, G. Mobbili, L. Sorci, R. Galeazzi, C. Minnelli, Mechanistic insight toward EGFR activation induced by ATP: role of mutations and water in ATP binding patterns, J. Biomol. Struct. Dyn. 41 (2023) 6492–6501, https://doi.org/10.1080/07391102.2022.2108497.
[61] J. Huang, S. Rauscher, G. Nawrocki, T. Ran, M. Feig, B.L. De Groot, et al., CHARMM36m: an improved force field for folded and intrinsically disordered proteins, Nat. Methods 14 (2016) 71–73, https://doi.org/10.1038/nmeth.4067.
[62] S. Páll, B. Hess, A flexible algorithm for calculating pair interactions on SIMD architectures, Comput. Phys. Commun. 184 (2013) 2641–2650, https://doi.org/10.1016/j.cpc.2013.06.003.
[63] S. Nosé, A unified formulation of the constant temperature molecular dynamics methods, J. Chem. Phys. 81 (1984) 511–519, https://doi.org/10.1063/1.447334.
[64] M. Parrinello, A. Rahman, Polymorphic transitions in single crystals: a new molecular dynamics method, J. Appl. Phys. 52 (1981) 7182–7190, https://doi.org/10.1063/1.328693.
[65] D. Van Der Spoel, E. Lindahl, B. Hess, G. Groenhof, A.E. Mark, H.J.C. Berendsen, GROMACS: fast, flexible, and free, J. Comput. Chem. 26 (2005) 1701–1718, https://doi.org/10.1002/jcc.20291.
[66] M.J. Abraham, T. Murtola, R. Schulz, S. Páll, J.C. Smith, B. Hess, et al., Gromacs: high performance molecular simulations through multi-level parallelism from laptops to supercomputers, SoftwareX 1–2 (2015) 19–25, https://doi.org/10.1016/j.softx.2015.06.001.
[67] W. Humphrey, A. Dalke, Schulten K, VMD, Visual Molecular Dynamics, 1996.
[68] C. Minnelli, L. Cianfruglia, E. Laudadio, G. Mobbili, R. Galeazzi, T. Armeni, Effect of epigallocatechin-3-gallate on egfr signaling and migration in non-small cell lung cancer, Int. J. Mol. Sci. (2021) 22, https://doi.org/10.3390/ijms222111833.
[69] R. Adato, H. Altug, In-situ ultra-sensitive infrared absorption spectroscopy of biomolecule interactions in real time with plasmonic nanoantennas, Nat. Commun. (2013) 4, https://doi.org/10.1038/ncomms3154.
[70] G. Birarda, L. Vaccari, I. Cudin, M. Altissimo, E. Karantzoulis, D. Castronovo, et al., Preliminary simulations of SISSI infrared beamline at Elettra 2.0 diffraction limited storage ring, Nucl. Inst. Methods Phys. Res. B (2023) 545, https://doi.org/10.1016/j.nimb.2023.165150.
[71] M. Toplak, S.T. Read, C. Sandt, F. Borondics, Quasar: easy machine learning for biospectroscopy, Cells (2021) 10, https://doi.org/10.3390/cells10092300.
[72] M. Toplak, G. Birarda, S. Read, C. Sandt, S.M. Rosendahl, L. Vaccari, et al., Infrared Orange: connecting hyperspectral data with machine learning, Synchrotron Radiat News 30 (2017) 40–45, https://doi.org/10.1080/08940886.2017.1338424.
[73] Origin(Pro), Version Number (Version 2024). OriginLab Corporation, Northampton, MA, USA. n.d.